8.12

Combined Atomistic and Continuum Simulation of Fracture and Corrosion

SX0005

H. TAN

Louisiana State University, Baton Rouge, LA, USA

8.12.1   INTRODUCTION

SX0010   Combined atomistic and continuum simulation plays an important role in nanomechanics because of three reasons: multiscale failure behaviors, ever-limited computational resources even though they are much powerful than before, and insufficient experimental information at the atomistic scale. Continuum theory by itself is insufficient to explain nanoscale observations. Materials have atomistic scale structures that affect their macroscopic behavior. Though it is fundamental, atomistic vision of material behavior is limited by the computational possibilities.

SX0015   Fracture involves phenomena occurring at a range of length scales. While a crack propagates in the macroscopic scale, the crack tip always involves atomic scale behavior of successive atomic debonding. With modern computers the atomistic simulation tends to larger scale and continuum simulation goes to smaller scale. Continuum method is excellent in describing the large field. However, the approach generally represents an averaged characteristic. It gives an incomplete prediction of the local state of a nanoscale structure. Studies at the atomistic level are needed to understand the exact nature of the crack-tip responses. The requirement is a proper description of the interatomic potential.

SX0020   In corrosion science, traditional electrochemical, surface analytical, and spectroscopic studies gave only integral information on electrochemical processes occurring at solid/liquid interfaces. Local atomistic events and the influences of surface imperfections on the interfacial processes could not be directly analyzed. Interatomic forces often determine macroscopic phenomena in corrosion. The more or less hypothetical interpretation of integral results in terms of local atomic phenomena requires combined simulations to understand corrosion and corrosion inhibition reactions on an atomic level. Molecular simulations, such as lattice-gas Monte Carlo (MC), are best suited to model intermolecular forces along with their influence on corrosion kinetics. However, a major disadvantage of MC simulations is their computational intensity that limits calculations to small length scales and short times. In contrast, many experimental techniques in corrosion science are limited to micrometers, and real systems are of even larger macroscopic length scales.

SX0025   Continuing improvements in high-performance computing over the last decade have made it possible to carry out atomic-scale simulations of material failure processes including fracture and corrosion. Technology now promises the great advance in computing power towards teraflop and even petaflop speeds employing very large parallel machines. On this new generation of computers, simulations can be carried out for systems thousand times larger or over timescales thousand times longer than previously engaged, permitting performing trillion-atom simulations to include the effects of microstructures that span diverse length scales up to the mesoscale regime above micron. However, because of system-size constraints even the fastest algorithms available for such atomistic models cannot represent the whole multiscale picture.

SX0030   In microscopic scale atomistic models, simulations are required to properly capture the spatiotemporal evolution of pattern formation. In macroscopic scales, continuum-type partial differential equations are typically used to describe the conservation equations of continuity, momentum, energy, and species. For the practical needs of the engineer trying to prevent material failure, the simulation of real material behavior on much larger space scales must be realized. One way to achieve this is by bringing together continuum and atomistic descriptions of matter into a seamless union. This chapter covers topics in combined atomistic and continuum simulation for structure failure including fracture and corrosion. It focuses on numerical methods dealing with the bridging in length and time scales. Other important issues in nanoscale simulations, such as potential construction and choices, are not included.

8.12.2   NANOSCALE BEHAVIORS

SX0035   There are processes on macroscopic length scales that, for fundamental reasons, cannot be described by continuum theory. They must be treated on the discrete atomistic scale. Famous examples of such processes include the dynamic fracture instability, intersonic crack motion, dynamic competition of dislocation emission and cleavage, atomic inertial effect, chaotic atom motion at the crack tip, stress-corrosion cracking, point defects and radiation damage, pitting corrosion, etc. The increasing

power of high-speed computation has made a major impact on studying material behaviors. Phillips (2001) systematically examined recent efforts that treat problems involving multiple spatial and temporal scales simultaneously.

8.12.2.1 Dynamic Fracture Instability

SX0040   There is a long-standing problem in the dynamics of fracture. Cracks in brittle materials are supposed to accelerate up to the Rayleigh wave speed according to theory, while experiments seldom show them exceeding half this speed. The problem is actually about energy balance. Cracks suddenly cost much more energy to propagate as they exceed a critical speed on the order of half the theoretical limit. Continuum fracture theory typically assumes that cracks are smooth. An initially smooth and mirror-like fracturing face begins to appear misty beyond a speed of about one-third the Rayleigh speed and then evolves into a rough, hackled region as the crack accelerates to a limiting velocity of about six-tenths the Rayleigh speed. The origin of the disagreement between theory and experiment suggests questions of microscopic impurities or imperfections in the material, experimental uncertainties, or failure of theory. All of these features cannot be explained using continuum theory, and experiment suggests a crack-instability beyond one-third of the Rayleigh wave speed (Fineberg *et al.*, 1991, 1992).

Abraham (2001) reported that fracture   SX0045 dynamics shows instability in the straight-line motion at one-third of the Rayleigh wave speed from a two-dimensional (2D) molecular dynamics (MD) simulation (Figure 1). A brittle crack initially propagates in a straight line and leaves mirror-like cleaved surfaces. However, at the crack speed of one-third of the Rayleigh wave speed (second image), the crack begins to roughen, and then to oscillate back and forth (third image) achieving a forward speed equal to approximately two-thirds of the Rayleigh speed. Similarly, for speeds less than one-third of the Rayleigh speed, the acceleration of the crack tip is quite smooth; however, the

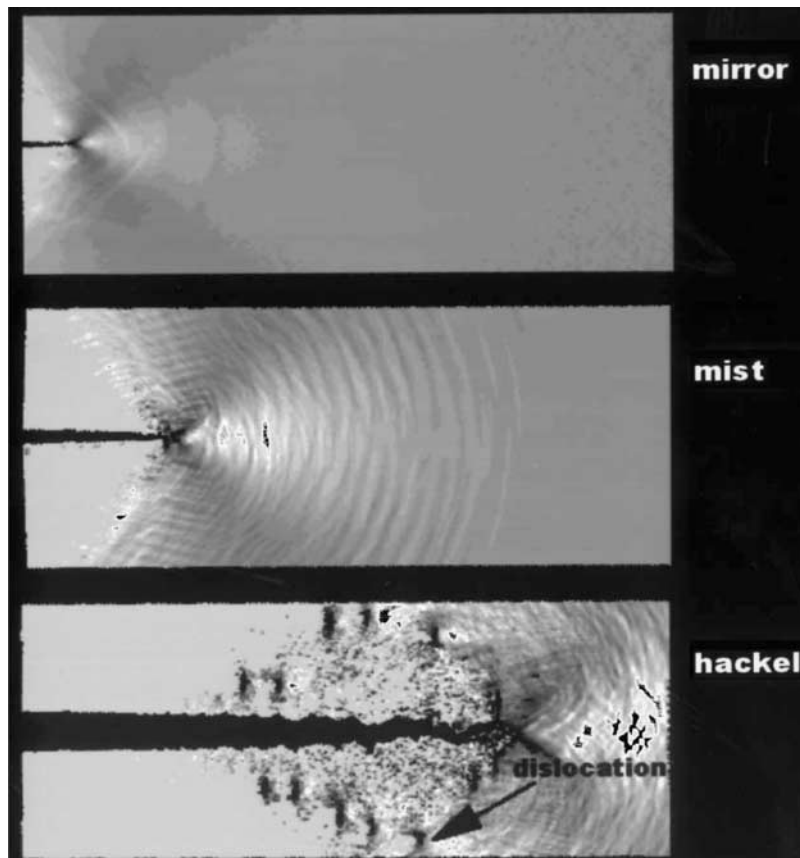**Figure 1** The dynamic regimes of brittle fracture in a two million atoms MD simulation. The brittle crack initially propagates in a straight line and leaves mirror cleaved surfaces. At the crack speed of one-third of the Rayleigh wave speed (the second image), the crack begins to roughen, and then to oscillate back and forth (the third image) achieving a forward speed equal to two-thirds of the Rayleigh speed (after Abraham, 2001).

instantaneous tip speed becomes very erratic after reaching one-third of the Rayleigh speed. This transition from smooth, mirror-like motion to rough, erratic motion signals the instability in the dynamics of the crack.

SX0050   Dislocations appear after the onset of the instability and are apparent in the gray-scale pictures. The spacing between these dislocations is quite regular. There are also delays in the zigzagging of the crack that must be accounted for and which further reduces the speed estimated by simple geometry. If crack zigzagging can be prevented, its forward motion would be much faster and maybe equal to the Rayleigh speed. Abraham *et al.* (1994, 1997a, 1997b) discussed this issue in detail through atomic simulations.

8.12.2.2   Dislocations Emission and Cleavage Competition

SX0055   Dynamic dislocations are observed emitting from the crack front in large-scale MD simulations. Tan and Yang (1994a) and Zhang and Wang (1995) simulated the nucleation and emission of dislocations by MD method. The sequence of dislocation emission events, essential for establishing an intrinsic ductility criterion, strongly depends on the crystallographic orientation of the crack front (Zhou *et al.*, 1997). Branching follows dislocation emission along a slip plane. The branching instability requires the crack to achieve a critical velocity, as well as an induction time for energy buildup at the crack tip (Zhou *et al.*, 1996). Tang and Wang (1999) simulated the behavior of a crack in body-centered-cubic metal Mo under different loads and observed dislocation emissions near the crack tip.

SX0060   Through MD simulations in nanoscale fracture, Tan and Yang (1994a) established a critical rate theory for the competition between dislocation emission and cleavage. Figure 2 defines four different loading histories. Those loading histories lead to different atomistic fracture patterns after 12 ps of loading. When the loading magnitude is low, the fracture process is dominated by dislocation emission insensitive to the loading rates. For the same material under high loading magnitude, however, the atomistic failure patterns shift from dislocation emission to cleavage as the loading rate increases. They explain the above observations by the following *critical rate theory*. For a given solid aggregate, there exist three material parameters characterizing the cleavage vs. dislocation emission response near a nanoscale shape crack tip. They are: K_{emit}, the K field at which the crack begins to emit dislocations; K_{cleave}, the critical K value at which a nanoscale

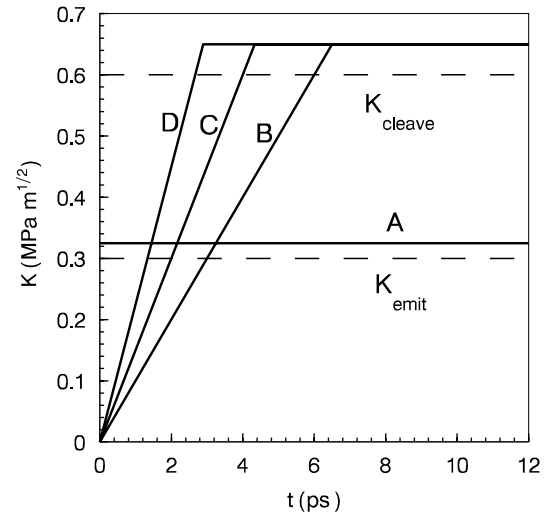**Figure 2** Four loading histories: (A) $\dot{K} = \infty$, $K_{max} = 0.325 \text{ MPa m}^{1/2}$; (B) $\dot{K} = 0.1 \text{ MPa m}^{1/2} \text{ ps}^{-1}$, $K_{max} = 0.65 \text{ MPa m}^{1/2}$; (C) $\dot{K} = 0.15 \text{ MPa m}^{1/2} \text{ ps}^{-1}$, $K_{max} = 0.65 \text{ MPa m}^{1/2}$; (D) $\dot{K} = 0.225 \text{ MPa m}^{1/2} \text{ ps}^{-1}$, $K_{max} = 0.65 \text{ MPa m}^{1/2}$ (after Tan and Yang, 1994a).

shape crack begins to cleave; and T_{nu}, incubation time to nucleate a dislocation from the crack tip. The value of K_{emit} is lower than that of K_{cleave} for most metals. For aluminum, the atomistic simulation suggests the following values: $K_{cleave} = 0.6 \text{ MPa m}^{1/2}$, $K_{emit} = 0.5 K_{cleave}$, and $T_{nu} = 2 \text{ ps}$. A dislocation emits from the crack tip at a velocity of $\sim 1{,}000 \text{ m s}^{-1}$ in aluminum, and an apparent complete dislocation is formed only at several Burgers vectors away from the crack tip. The time elapse for a dislocation to pass over one interatomic distance is 0.4 ps, which is only a fraction of T_{nu}.

SX0065   When K applied is below K_{emit}, the material only sustains elastic deformation. When K is raised above K_{emit} but still below K_{cleave}, dislocations emit from the crack tip and loading rate has little effect on the fracture process. When K is above K_{cleave}, however, the loading rate begins to control the fracture process and the ductility in the nanoscopic core. A critical loading rate, $\dot{K}_c$, is introduced as

$$\dot{K}_c = \frac{K_{cleave} - K_{emit}}{T_{nu}} \qquad (1)$$

If the loading rate $\dot{K}$ is less than $\dot{K}_c$, the crack tip has enough time to generate dislocations after K surpasses K_{emit}. As shown in Figure 3(a), dislocation emissions sufficiently blunt the crack tip before the apparent value of K reaches K_{cleave}, and the material behaves nanoscopically ductile. The ductility is reduced
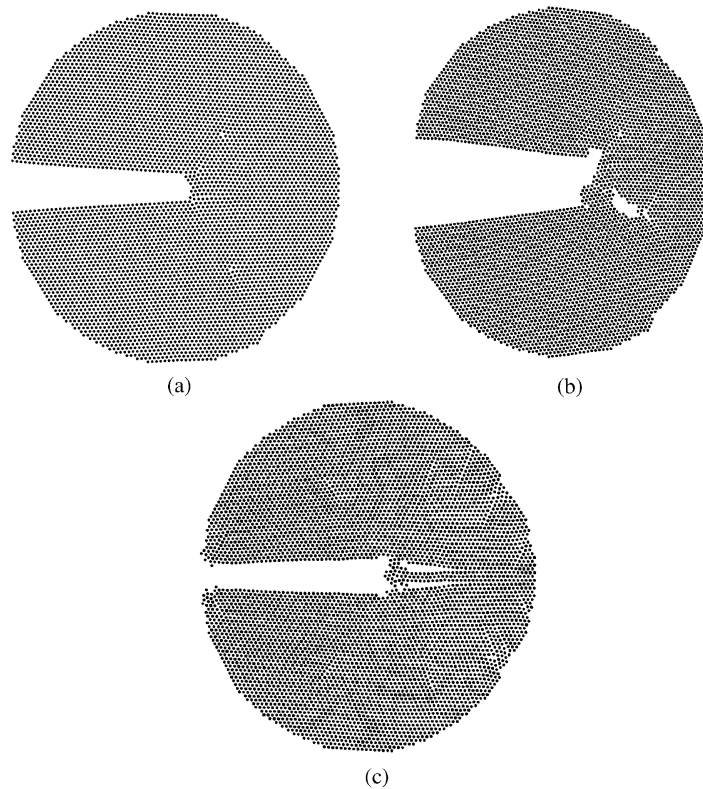
Figure 3 Atomistic fracture patterns of pure aluminum under the loading rates and loading magnitudes described in the above figure. Simulation time is 12 ps (after Tan and Yang, 1994a).

when higher loading rates are imposed. When $\dot{K}$ is close to $\dot{K}_c$ (loading history C in Figure 2), the nanoscopic crack-tip configuration shifts from ductile to brittle. Figure 3(b) shows the co-existence of dislocations and cleavage embryos. If the loading rate $\dot{K}$ is higher than $\dot{K}_c$, the crack cleave when the load K shoots from K_{emit} to K_{cleave} before a dislocation has time to emit from the crack-tip, as shown in Figure 3(c). As the material begins to cleave, the dislocation emission is suppressed, and premature dislocations are left behind the cleavage tip. Cleavage proceeds much faster than the dislocation nucleation. In fact, cleavage advances 4–5 bonds per picosecond (1,600–2,000 m s^{-1}) when K is above K_{cleave}, while dislocation nucleation needs 2 ps. Eight to 10 bonds ahead of the crack tip will be broken before a dislocation may emit from the original crack tip, and the fracture response is brittle. Consequently, the critical loading rate in Equation (1) plays an important role in dynamic ductile-to-brittle transition.

When atomistic simulations go to a large-scale the results can be compared with experimental test. Horstemeyer *et al.* (2001a, 2001b, 2002) performed large deformation MD calculations using the embedded atom method to investigate the material plasticity at highly applied strain rate (10^6–10^{12} s^{-1}). The increase of flow stress at increasing strain rates results from phonon drag. The simulations agree well with the experiments using interfacial force microscopy and nanoindentation test.

When atomistic simulations go to a large-scale the results can be compared with theoretical analysis. For the transient nature of dislocation emission from a crack tip, Yang *et al.* (2001) examined the issue from continuum mechanics aspect and demonstrated the phenomena from a clear mathematical analysis. It should be mentioned that there are other possibilities to bridge the scale. Beltz and Lipkin (2000) showed that discrete dislocation theories could be exploited to explain certain fracture phenomena in a way that links theories appropriate for vastly differing length scales.

8.12.2.3 Intersonic Crack Motion

Abraham and Gao (2000) performed atomic simulations of crack propagation along a weak interface joining two harmonic crystals. The simulations show that a mode II shear dominated crack can accelerate to the Rayleigh wave speed and then nucleate an intersonic

daughter crack that travels at the longitudinal wave speed. Gao *et al.* (2001) studied mechanisms of intersonic crack propagation under shear dominated loading by both MD and continuum elastodynamics methods. A MD simulation gave the mechanism for a mode II crack "jumping" over the forbidden velocity zone (Figure 4) where a series of color maps of the shear stress component is used to reveal the details of this process. This transition occurs by the nucleation of an intersonic daughter crack ahead of the mother crack traveling at nearly the Rayleigh wave speed.

SX0090   As the mother crack approaches the critical state of nucleation, the crack tip region is asymmetrically distorted with a bulge on the right side of the crack face, as shown in Figure 4(a). The linear elastic solutions of dynamic crack tip field (Freund, 1990) predict that the opening displacements along the crack face are symmetric with respect to the crack line under mode I loading and zero under mode II loading.
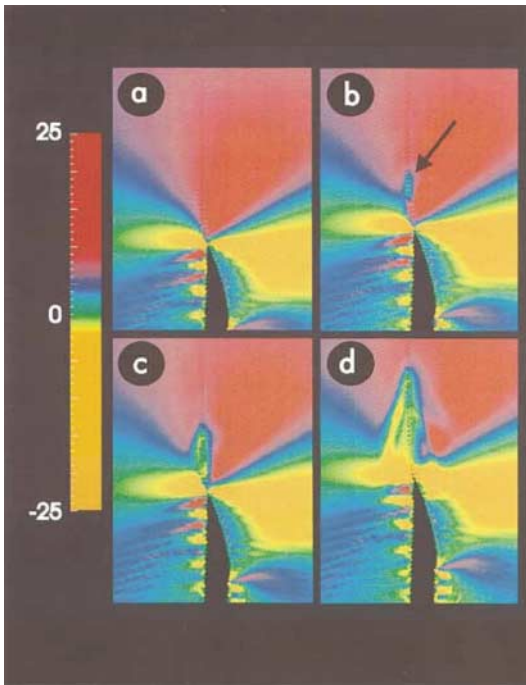

Figure 4 Nucleation of intersonic daughter crack at the mother crack. The figures represent a progression in time from (a) through (d). (a) The approach of the critical state for the mother crack. Note the asymmetrically distorted crack-tip region. (b) The birth of the intersonic crack. A very sharp slit is born ahead of the tip of the mother crack. (c and d) The daughter crack joins the mother crack and quickly approaches the longitudinal sound speed. The color bar shows the color map for the shear stress component. The bulged mother crack is still propagating at the Rayleigh wave speed (after Gao *et al.*, 2001).

There is only slip-like motion of crack surfaces under mode II situation. According to these solutions, the crack opening displacements should remain symmetric even under mixed mode conditions, which is inconsistent with the asymmetric distortion observed in the simulation. Figures 4(b)–(d) show the detailed process of the birth of the intersonic daughter crack. It is seen that a sharp intersonic crack is nucleated at a small distance ahead of the mother crack.

The MD simulations demonstrate intersonic   SX0095 crack propagation and the existence of a "mother"–"daughter" crack mechanism for a subsonic shear crack to jump over the forbidden velocity zone. This mechanism is reminiscent of the Burridge–Andrews mechanism (Burridge, 1973; Andrews, 1976; Burridge *et al.*, 1979) based on continuum theories, although the continuum description cannot provide an *ab initio* description for crack formation, and the details of crack-tip distortion are not consistent with the continuum solutions. The birth of the daughter crack cannot be characterized by a critical energy release rate or a critical stress intensity factor near the mother crack because both these quantities vanish at the Rayleigh wave speed. It seems that the only possible mechanism by which the daughter crack can be nucleated is by the finite stress peak ahead of the mother crack, and along the weak bonding line, as measured in the stress field and discussed by Burridge (1973).

Large-scale atomistic simulation is becoming   SX0100 mature and can be compared with analytical results. Guo *et al.* (2002) gave analytical solutions for a sub-Rayleigh or an intersonic crack accelerating or decelerating to a different (sub-Rayleigh or intersonic) cracking speed. Numerical simulations and theoretical analyses describe the problem from different point of view and still give the similar results.

8.12.2.4 Atomic Inertial Effect

The important difference between continuum and MD models is the role of inertia,   SX0105 which dominates in the atomistic models. The transition from a stationary to a moving crack, as a function of the applied driving force, occurs continuously in continuum models (Freund, 1990). However, in atomistic models with strong short-ranged bonds the transition is discontinuous and exhibits hysteresis as a function of the driving force (Langer, 1992; Ching *et al.*, 1995; Fisher *et al.*, 1997; Persson, 1998). The absence of atomic inertia effects in continuum models cause this difference.

Tan and Yang (1995) devised a simplified   SX0110 combined atomistic and continuum model, the crack-tip atom string model (Figure 5), to

Continuum

K_{II}
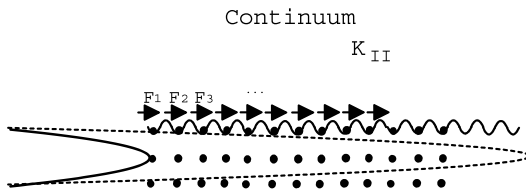
F_1 F_2 F_3 ...

Figure 5 Crack-tip atom string model. The crack is viewed as a semi-infinite slit in an otherwise unbounded solid, with mode II loading applied at infinity through a crack-tip singularity field described by K_{II}. N columns of atoms ahead of the crack tip are considered (after Tan and Yang, 1995).

analyze the mass effect on nonlinear motion of atoms during dislocation emission processes. In the figure, the continuum exerts force F_i and constraint to the sliding atom i, under the framework of linear fracture mechanics. The results show that the dislocation emissions are inherently transient; a dislocation is formed near the crack tip by an atomistic catastrophic process, and the sudden release of energy sets the dislocation in transient motion. The occurrence of chaos initiates the emission process of a dislocation. Cloud-like motion of the dislocation core position ahead of the crack tip is revealed. Similar models were used to study nonlinear crack-tip atom motion during cleavage (Tan and Yang, 1996a) and fracto-emission (Tan and Yang, 1996b).

8.12.2.5 Stress-corrosion Cracking

SX0115   Stress-corrosion cracking (SCC) is a term used to describe service failures in engineering materials that occur by slow, environmentally induced crack propagation. The observed crack propagation is the result of the combined and synergistic interaction of mechanical stress and atomic reactions. Atomistic simulations of SCC become more and more realistic. During fracture, sufficiently strong mechanical forces separate atoms that are chemically bonded. In this sense fracture may be regarded as some kind of "mechanical chemistry" and it is most natural that the environment, if it contains reactive molecules, influences fracture. The mechanics of growing cracks with their singular stress and strain fields and strongly nonlinear material behavior is intermingled with the chemical action of adsorbing and diffusing chemical species. See Section 8.12.4.7 on numerical simulations of hydrogen–dislocation interaction.

8.12.2.6 Point Defects and Radiation Damage

SX0120   The energetics of point defects provides the controlling factor in determining the atomistic

mechanisms in a wide range of solid-state processes. Varied approaches were followed in the past in modeling the relevant perfect crystals for interatomic forces of nonionic solids and potentials for ionic materials. MD has been applied to problems with point defects. Embrittlement of ferritic steels due to long-term neutron irradiation is one of the most important issues facing the nuclear power industry today. Identifying the mechanisms of embrittlement is a key requirement to guarantee the safety and economic viability of operating light-water reactors.

SX0125   In the study of radiation damage, MD simulations have played a very important role in understanding the details of defect production in displacement cascades, and in helping to construct empirical models. Extensive reviews of recent MD simulations of radiation damage can be found in Jaraiz *et al.* (1996). At a sufficiently high temperature and over long time scales, the defects generated by the displacement cascade interact and migrate over long distances. One of the key quantities required to make quantitative predictions of microstructure evolution in irradiated materials, and to extrapolate the results of experiments on model systems to actual operating conditions, is the fraction of freely migrating defects, that is the fraction of produced defects that can escape recombination reactions within their nascent cascade to migrate freely through the lattice. This fraction strongly depends on the form of the primary damage state, and on the relative mobility of the various point defects and defect clusters produced by the cascade.

SX0130   From a simulation perspective, although MD techniques can be used to study the structure and the initial evolution of the as-produced damage, the computational time becomes prohibitive beyond the first few nanoseconds, even for state-of-the-art scalable parallel machines. To overcome these limitations, a way of connecting the MD simulation results to other simulation methods such as rate theory (Phythian *et al.*, 1995) or kinetic MC simulations (for example, Heinisch, 1995; Heinisch and Singh, 1996; Jaraiz *et al.*, 1996) is required. In particular, MC simulations appear very promising because they provide the ability to perform atomic-level simulations of the defect kinetics and microstructural evolution over relevant length and time scales.

SX0135   Radiation-induced microstructural and compositional changes in solids are governed by the interaction between the fraction of defects that escape their nascent cascade and the material. Soneda and Rubia (1998) used a combination of MD and kinetic MC simulations to calculate the damage production

Mobile defects can escape from kMC box

MD computation box
(max: 17x17x17nm)

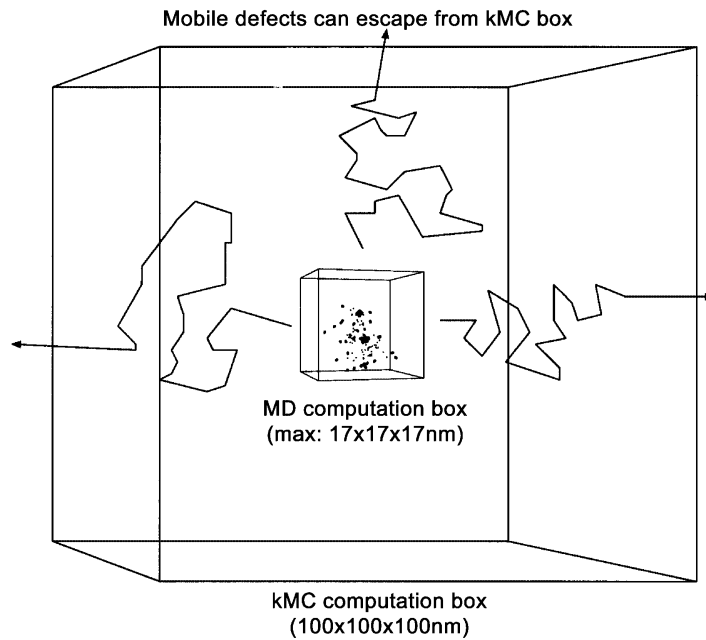kMC computation box
(100x100x100nm)

Figure 6 Schematic view of the computational box for the KMC simulations. The MD cascade simulation results are placed at the center of the KMC box. The dimensions are 17 nm × 17 nm × 17 nm for the MD box and 100 nm × 100 nm × 100 nm for the KMC box (after Soneda and Rubia, 1998).

efficiency and the fraction of freely migrating defects in α-Fe at 600 K. As shown in Figure 6, MD simulations provide information on the nature of the primary damage state as a function of recoil energy, and on the kinetics and energetics of point defects and small defect clusters. The kinetic MC simulations serve as the input of the MD calculations and provide a description of defect diffusion and interaction over long time and length scales.

8.12.2.7 Pitting Corrosion

Pitting corrosion is a localized corrosion that is exceedingly aggressive, since it does not extend over the metal surface and tends to penetrate into the interior that causes the majority of failures in metallic structures. Pitting corrosion of an initially passivated (oxide-covered) metal in contact with anionic aqueous solutions is normally triggered by the localized breakdown of the extremely thin (~ 1 nm thick) and highly stable passivating layers. Due to its intrinsic localized nature, this starting episode is commonly considered as a sporadic and stochastic event. This random nature manifests itself both in the distribution of induction times, i.e., the onset time for pit initiation, or in the generation of fluctuations in the free potential and, most frequently, of the current at constant applied potential. It is difficult to experimentally observe the atomistic nature of the fluid/metal interface.

Cl⁻ (a)

M^{v+} (b)

MCl_v layer (c)

(d)
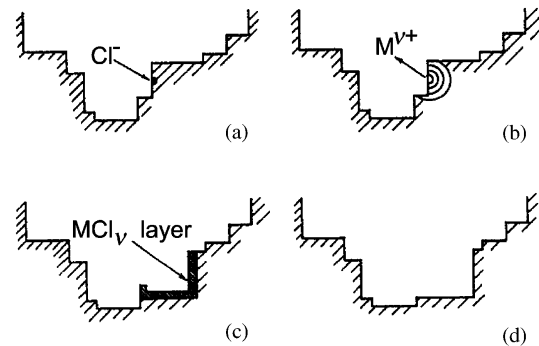
Figure 7 A schematic representation of the progress of a tunneling event: (a) pit nucleation; (b) oxidation advance; (c) slowing down of the tunnel growth due to the formation of a salt layer; and (d) final stage of the tunnel realization (after Reigada *et al.*, 1994).

Reigada *et al.* (1994) developed a MC simulation model for pitting corrosion that intrinsically incorporated the statistical nature of the process to analyze both electrochemical responses and morphological features of the growing pits. Figure 7 shows the simulation on tunneling mechanism for localized pitting corrosion. Once initiated from a more or less semicircular nucleus, the tunnel progresses by metallic dissolution in a burst-like way, turning into a crystallographic front as the local oxidation is progressively completed.

Strobel *et al.* (2001) simulated the ion erosion of FCC (1 1 1) surfaces. In a fully 3D

kinetic lattice MC model thermodynamically activated processes like adatom, step-edge, or surface vacancy diffusion are combined with ballistic effects due to single ion impacts, i.e., sputtering, adatom, and surface vacancy generation. In the course of erosion nucleation of surface vacancy islands, their growth, both laterally and vertically, and subsequent coarsening of these pits is observed.

8.12.3 SIZE EFFECTS

SX0155   In investigating fracture and corrosion behaviors at different size scales, it is desired to bridge concepts from the continuum to the atom. Continuum mechanics is founded on the assumption that the spatial variations in a given field variable are sufficiently slow as to make possible the smearing out of the atomistic degrees of freedom upon which they are founded. Many nanoscale problems cannot get answered only from continuum point of view. The problem arises from the continuum assumption of material. Length scale comes into the continuum equations in nanoscale. The length scale problem also exists in mesoscale (see Needleman, 2000 for computational mechanics in that scale).

8.12.3.1 Elastic Solids with Holes

SX0160   Lamé's classical solution for an elastic 2D plate, with a hole of radius a and uniform tensile stress σ_0 applied at the far field, gives the stresses distribution expressed in cylindrical polar coordinates as

$$\begin{aligned}\sigma_r &= \sigma_0\left(1 - a^2/r^2\right) \\ \sigma_\theta &= \sigma_0\left(1 + a^2/r^2\right)\end{aligned} \qquad (2)$$

for $a \leq r < \infty$, $0 \leq \theta < 2\pi$, where r is the distance to the center of the hole. The companion shear stress component is zero by virtue of the axisymmetry of the configuration. Setting $r = a$ in σ_θ reveals a stress concentration factor (SCF) of two at the edge of the hole. Consider what happened to this concentration factor if $a \rightarrow 0$. The SCF is independent of a, so it remains equal to two even when the hole disappears. This is inconsistent with what one would expect physically, namely that the limit $a \rightarrow 0$ should be the same as when the plate is whole without a hole and has no stress concentration. What is missing in the classical statements of Lamé's hole problems is the recognition that atoms or molecules on opposite sides of any hole must start to interact with each other as the hole closes. This interaction produces cohesive stresses on walls of the hole.

Sinclair and Meda (2001) provided a cohesive stress model and introduced a length scale parameter, the equilibrium separation of the atoms or molecules comprising the plate.

Horstemeyer *et al.* (2001b) examined the size   SX0165 scale effects on single-crystal FCC metals with MD simulations on single-crystal nickel ranging from 100 atoms to 100 million atoms. They found that plasticity as reflected by the global averaged stress–strain behavior is characterized by four different length scales: (i) below 10^4 atoms, (ii) between 10^4 atoms and 10^6 atoms ($2\,\mu m$), (iii) between $2\,\mu m$ and $300\,\mu m$, and (iv) above $300\,\mu m$.

8.12.3.2 Evolution of Surface Roughness

Surface roughening of long wavelength can   SX0170 be modeled with continuum energetics and kinetics. In continuum models the tendency of the surface to change the shape of its reference configuration is represented by the total chemical potential variation with respect to admissible variation of the surface configuration. A positive surface energy tends to flatten the surface, while a positive strain energy is inclined to roughen the surface, lowering the chemical potential. This competition depends on the special frequency of the surface roughness. Kim *et al.* (1999) built the evolution of surface-roughness spectrum theory. As shown in Figure 8, they found that when chemical etching applied to a stressed surface, there comes a length scale, namely the critical wavelength

$$\lambda_{\mathrm{cr}} = \frac{2\pi\mu\gamma}{(1 - v)\sigma^2} \qquad (3)$$

where γ is the surface energy density, μ is the shear modulus, and v is Poisson's ratio. For the evolution of surface roughness with a shallow chemical etching, the surface roughness grows with spatial wavelength $\lambda > \lambda_{\mathrm{cr}}$, and decays with $\lambda < \lambda_{\mathrm{cr}}$.

Zhang and Bower (1999) carried out 3D   SX0175 numerical simulations of island formation in a strained layer epitaxial system. The simulation showed a similar size scale dependent phenomenon in the surface diffusion driven deformation of thin films.

The stress-induced roughening of solid   SX0180 surfaces is considered to be the main cause of failure process in MEMS devices (Kim and Hurtado, 2000). Using a general kinetic law, Yu and Suo (2000), and Liang and Suo (2001) developed a linear perturbation analysis to compute the evolution of the shape of the interface. Prevost *et al.* (2001) formulated a finite element (FE) method to simulate the
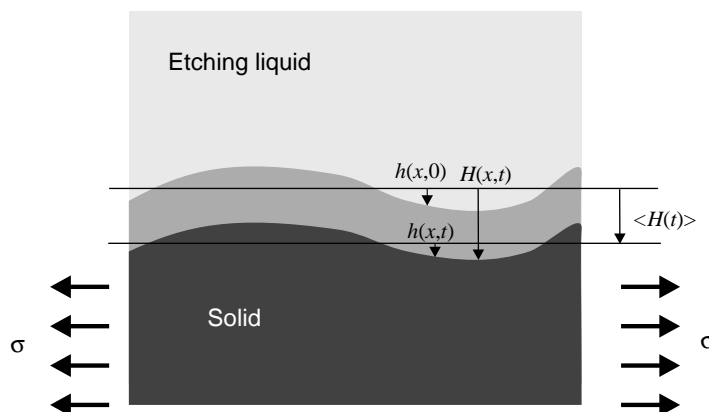
Figure 8 Schematic of chemical etching of a solid surface under stress. The height and roughness of the surface, at time *t* and position *x*, are represented as $\langle H(x,t) \rangle$ and $H(x,t)$, respectively (after Kim *et al.*, 1999).

stress dependent surface reaction. Brok and Morel (2001) studied experimentally the effect of compressive elastic strain on the microstructure of free faces of stressed solids on soluble salt held in an aqueous solution.

8.12.3.3   Oxide Surfaces

SX0185   Oxide surfaces are technologically important in a range of applications, including catalysis, corrosion, gas sensors, ceramics, and high-temperature superconductivity. Nanophase materials have a large fraction of atoms in the interfacial regions, which have a dramatic effect on the structure and physical properties of these materials (Siegel, 1994; Stern *et al.*, 1995; Kalia *et al.*, 1997). Campbell *et al.* (1999) and Vashishta *et al.* (2001) studied the oxidation process of an aluminum nanocluster (diameter 200 Å) using MD simulations. They investigated the structural and dynamic correlations in the oxide region and the evolution of various quantities including surface oxide thickness, diffusivities of atoms, and local stresses. The simulation results, shown in Figure 9, gave the oxide thickness as a function of the simulation time. The oxide thickness increases linearly with time during the first 50 ps and subsequently the rate becomes smaller and the thickness saturates at 33 Å. The figure is a plot of the inner and outer radial extents of the oxide. The growth of the oxide scale is both inward and outward: inward because of the movement of oxygen towards the interior of the cluster and outward because of the movement of aluminum towards the oxide surface. The inward and outward growth of the oxide saturate at 77 Å and 110 Å, respectively, with the inward growth saturating later than the outward. Analysis of local stresses reveals large stress gradients throughout the nanocluster with the oxide largely under nega-
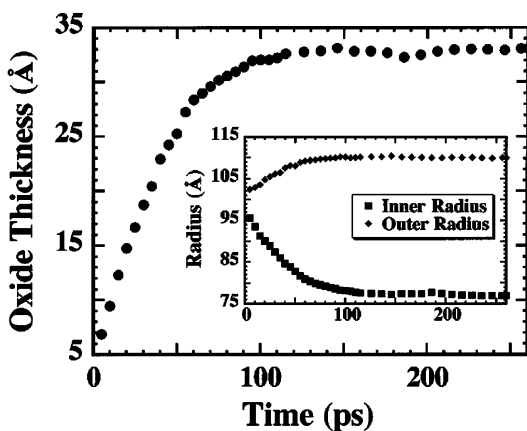
Figure 9   Thickness of the oxide layer as a function of simulation time. The inner and outer radial extents of the oxide layer as a function of simulation time are shown in the inset (after Campbell *et al.*, 1999).

tive pressure and the metal core under positive pressure. The large stress gradients give rise to diffusion of atoms in the oxide region. The radial and tangential diffusivities remain about equal, indicating that while the oxide grows in radial direction, high tangential diffusion causes uniformity in the oxide thickness with respect to polar angles (Figure 10).

Aluminum nanoclusters of diameters 100–700 Å are known to form an oxide scale with thickness between 20 Å and 50 Å in oxygen gases at room temperature (Suits *et al.*, 1995; Aumann *et al.*, 1995; Sánchez-López *et al.*, 1996, 1998; Nieh *et al.*, 1996). The thicknesses of oxide scales were measured (Sako *et al.*, 1990) as a function of cluster size for small metallic clusters. For aluminum clusters of diameter 200 Å the thickness is 30–40 Å. The MD simulations show remarkable similarity in the oxide thickness with the experimental   SX0190

Figure 10 Defect subspace. A set of bonds in the super-cell is altered, forming a "defect subspace" in the lattice. The number of such altered bonds is small comp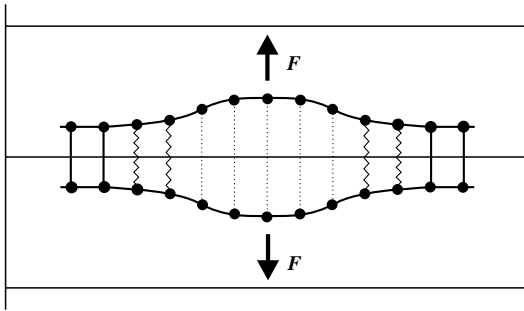ared to the number in the supercell. In the figure, a crack is represented by bond annihilation over a plane constituting the cleavage plane of the crack. Forces, *F*, are applied to the center of the crack, which provide the load on the crack. At the ends of the crack, a "cohesive zone" is defined over which nonlinear bond forces may be reconstituted, consistent with an assumed force law. Dotted lines in the figure correspond to bonds that have been annihilated, and wavy lines to bonds that have been first annihilated and then reattached with nonlinear bonds (after Thomson *et al.*, 1992).

observations. Subsequent MD simulations showed the detailed structural analysis of the oxide scale on aluminum nanoclusters.

SX0195   Dynamic charge transfer in the simulation gives rise to a computationally intensive Coulomb interaction which, for the number of atoms necessary in a realistic simulation, requires highly efficient algorithms that map well onto parallel architectures. The fast multipole method of Greengard and Rokhlin (1987) was applied for the long-range Coulomb interaction with extensions for stress calculations, and the multiple time-step algorithm of Tuckerman *et al.* (1990). Both algorithms are well suited to parallel architectures.

SX0200   Oxidation has a deleterious effect on the physical and mechanical properties of materials, including premature failure of otherwise properly designed systems. Using the MD approach, Campbell *et al.* (1999) studied effects of oxidation on fracture in aluminum. The simulation requires models of interatomic potentials that are much more refined than those used in conventional MD simulations. The variable-charge interatomic potential is used because it can handle bond formation and bond breakage (Streitz and Mintmire, 1994). For these simulations, Nakano (1997) developed a multilevel preconditioned conjugate-gradient method by splitting the Coulomb-interaction matrix into short- and long-range components. Multiresolution MD algorithm was realized on parallel computers (Nakano, 1993, 1994b, 1998a, 1998b, 1999; Kalia *et al.*, 1993).

8.12.4 MULTISCALE MODELING

Material failure is a process with information at several scales. The geometric complexity is complicated further by the interactions among structural features at different scales. In addition to the structural hierarchy of polycrystalline materials it is essential to recognize their dynamical nature. Processes at various length scales usually possess different relaxation times, suggesting that in addition to the spatial hierarchy a temporal one exists. Microstructures are only a reflection of the fact that a polycrystalline material has not had enough time to reach equilibrium. Also, microstructures are path and history dependent, adding further complexity to understanding and controlling their evolution.   SX0205

Combined atomistic and continuum simulation provide a basic tool in understanding multiscale material behaviors. The main idea in the coupled atomistic and continuum approach is to use atomistic modeling at places where the variation is on an atomic scale, and the continuum approach elsewhere. The challenging problem comes with the communication between two descriptions of the materials.   SX0210

8.12.4.1 Lattice Green's Function

Thomson *et al.* (1992), Zhou *et al.* (1993), and Schiøtz and Carlsson (1997) used lattice Green's function for calculating the static structure of defects in a lattice. In this approach, the actual number of atomic degrees of freedom is not changed, but rather a large proportion of the atoms are treated using a linear approximation to their response. These linear atoms, while they are still explicitly modeled, demand considerably less computational overhead than fully nonlinear atoms. Thus, this approach greatly reduces the calculation time. The 2D and 3D Green's function techniques newly developed by Rao *et al.* (1999) are used to relax the boundary forces in the simulations of cross-slipped core structures of $(a/2)[110]$ screw dislocations in modeling FCC structures.   SX0215

Imagine that an atom at the lattice point l' is given a displacement $u_j(l')$. The applied force F_i on atom at the lattice point l required to maintain the balance is given simply by   SX0220

$$F_i(l) = \phi_{ij}(l, l')u_j(l')$$
$$F = \Phi u \qquad (4)$$

where $\phi_{ij}(l, l')$, or "dynamic matrix," is defined as an appropriate second derivative of the total strain energy of the lattice, and is the balancing force in the i direction on an atom at the lattice point, l, because of an atom at the lattice point

l' is displaced a unit distance in *j*-direction. Inverting the equation yields

$$u_i(l) = g_{ij}(l, l')F_j(l')$$
$$u = \Phi^{-1}F = GF \qquad (5)$$

which identifies $g_{ij}(l, l')$ as the Green function matrix for the spring system.

In the perfect lattice,

$$\phi_{ij}(l, l') = \phi_{ij}(l - l') \qquad (6)$$

and

$$g_{ij}(l, l') = g_{ij}(l - l') \qquad (7)$$

because of the lattice translation symmetry. From

$$\phi_{ij}(l) = \frac{1}{8\pi^3 N^3} \sum_{k \in \text{B zone}} \phi_{ij}(k)\exp[-ik \cdot l] \qquad (8)$$

G can be easily obtained in k space,

$$\phi_{ij}(k) = \sum_{l \in \text{shell}} \phi_{ij}(l)\exp[-ik \cdot l] \qquad (9)$$

where "B zone" stands for Brillouin zone, and $\phi_{ij}(k)$ is understood to be the transform function of $\phi_{ij}(l)$.

The Green's function operator has a similar Fourier expansion, and the inversion of ϕ is simply

$$g_{ij}(k) = \left[\phi_{ij}(k)\right]^{-1} = \left[\sum_{l \in \text{shell}} \phi_{ij}(l)\exp[-ik \cdot l]\right]^{-1} \qquad (10)$$

Since ϕ is a 3×3 matrix in 3D situation, the right-hand side of the above equation requires the inversion of a small matrix for each value of k. Noting that $\phi_{ij}(k)$ in the above equation is the sum over the shell of atoms within the range of the force law, the perfect lattice Green's functions are easily determined numerically. When the inverse Fourier transformation is performed on $g_{ij}(k)$, the Green's function operator in real space, $g_{ij}(l)$, is determined.

In heterogeneous problems, the value of Φ is not the same for every lattice atom due to the broken strings (cracks) or modified springs, and so in principle the entire matrix Φ must be inverted to obtain the entire matrix G, which is a large numerical problem. Solving Equation (5) for G in a far more efficient manner is accomplished by the following procedure. First, the Φ and G for the perfect lattice of springs are calculated and denoted as Φ^0 and G^0. Since the perfect system is periodic, Fourier transformation technique can be utilized to calculate G^0. For the heterogeneous system of interest containing *n* defects, the force constant matrix Φ can be defined as

$$\Phi = \Phi^0 + \delta\Phi \qquad (11)$$

where $\delta\Phi$ is a matrix having only *n* entries that are coupled to the defects. G for the heterogeneous material can be solved in terms of G^0 and $\delta\Phi$ as

$$G = [I - G^0\delta\Phi]^{-1}G^0 = G^0 + G^0\delta\Phi G \qquad (12)$$

which is the so called Dyson's equation, with I being the unit matrix. With appropriate labeling of the atoms, one can arrange for all the entries in $\delta\Phi$, of which there are only $n \times n$ items for defects, to be in the upper left corner of the matrix,

$$\delta\Phi = \begin{pmatrix} \delta\Phi_p & 0 \\ 0 & 0 \end{pmatrix} \qquad (13)$$

Then, G and G^0 can be partitioned similarly as

$$G = \begin{pmatrix} G_{11} & G_{12} \\ G_{21} & G_{22} \end{pmatrix} \qquad (14)$$

and

$$G^0 = \begin{pmatrix} G_{11}^0 & G_{12}^0 \\ G_{21}^0 & G_{22}^0 \end{pmatrix} \qquad (15)$$

and hence Equation (12) can be written as four separate equations

$$\begin{aligned} G_{11} &= G_{11}^0 + G_{11}^0\delta\Phi_p G_{11} \\ G_{12} &= G_{12}^0 + G_{11}^0\delta\Phi_p G_{12} \\ G_{21} &= G_{21}^0 + G_{21}^0\delta\Phi_p G_{11} \\ G_{22} &= G_{22}^0 + G_{22}^0\delta\Phi_p G_{22} \end{aligned} \qquad (16)$$

In the separate equations, however, G_{11}, G_{11}^0, and $\delta\Phi$ are only matrices of size $n \times n$, and so the first equation can be solved for G_{11} by inversion of only an $n \times n$ matrix. The remaining components of the G matrix can be calculated by matrix multiplication. The major numerical requirement is the inversion of the $n \times n$ matrix but the result is the total G for a much larger system of atoms. Displacements and local spring forces are then calculated by applying Equation (5).

Green's functions generally are used for static systems. For a dynamic fracture MD simulation, the initial atomic structures of the crack are determined from the lattice Green's function method (Masuda-Jindo *et al.*, 2001).

8.12.4.2 FE and MD Handshaking

SX0255   To model defects with long-range stress fields atomistically, one should make sure that the boundary conditions applied to the atomistic region are appropriate. This means that either they have to be applied very far away from the defect that causes a lot of unnecessary computational effort, or some sort of flexible boundary conditions have to be applied. One way of doing the latter is to surround the atomistic region with a FE continuum.

SX0260   The atomic and the continuum regions are divided into two zones. Seamless coupling is required for combined FE/MD computations (Kohlhoff *et al.*, 1991; Hoover *et al.*, 1992; Tan and Yang, 1994a, 1994b; Yang *et al.*, 1994; Yang and Tan, 1996; Rafii-Tabar *et al.*, 1998; Abraham *et al.*, 1998; Nakano *et al.*, 2001). There are two methods to combine the MD and FE region, one is through the imaginary surface, the other is through the overlapping layer.

8.12.4.2.1 *Imaginary surface*

(i) Methodology

SX0265   This FE/MD coupling method attempts to avoid the use of forces in the coupling of FE and MD. A one-to-one correspondence of FE-nodes and atoms is required in the transition zone. Atoms and FE-nodes are coupled by mutual displacement boundary conditions using an imaginary surface. Equilibrium is guaranteed if the elastic constants in the continuum region match those of the atomistically modeled region.

SX0270   As shown in Figure 11, the imaginary surface is placed at the interface between the FE and MD regions. On both sides of this fiducial surface within a fixed distance equal to the range of the MD interatomic potential, FE mesh points are placed at the equilibrium position of the MD atoms. An assumption is made that there is no diffusion at the FE/MD interface, so that atoms remain near the corresponding mesh points on either sides of this interface. This assumption makes artificial constraints on the atomic system so that no atomic defects can move across the continuum–atomistic interface. Moving away from the handshaking region into the FE region, the mesh spacing may be made larger. This is the principal reason that the FE algorithm is computationally efficient.

SX0275   An example is applying hybrid FE/MD method to simulate silicon and quartz microsystems. Empirical potentials by Stillinger and Weber (1985) and Vashishta (Nakano *et al.*,

MD/FE interface

FE Region   MD Region

MD/FE Region
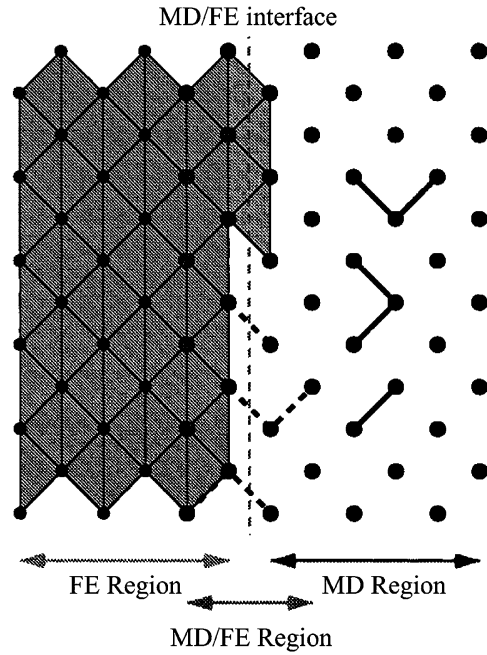
Figure 11 Illustration of FE/MD handshaking couplings for the crack simulation, with only a few representative MD examples shown. The FE/MD fiducial interface is the dashed vertical line. FE elements contributing to the overall Hamiltonian with full weight have dark shading; those contributing with half weight have light shading. Two- and three-body atomic interactions crossing fiducial interface also carry half weight, and are shown with dotted lines (after Rudd and Broughton, 2000).

1994a) are used in these simulations. They involve both two- and three-body interatomic terms:

$$V_{\text{MD}} = \sum_{i<j} V^{(2)}(r_{ij}) + \sum_{i,(j<k)} V^{(3)}(r_{ij}, r_{ik}) \quad (17)$$

The potential in the continuum FE system is

$$V_{\text{FE}} = \frac{1}{2} \sum_{m=1}^{N_{\text{cell}}} \sum_{p,q=1}^{p_{\max}} u_p^m K_{pq}^m u_q^m \qquad (18)$$

where the indices p and q run over the $p_{\max} = 6$ degrees of freedom associated with the 2D displacements at the three apexes of a triangular element, and $p_{\max} = 12$ degrees of freedom of 3D displacements at the four apexes of a tetrahedron.

     Rudd and Broughton (2000) differ from the prior work in the dynamics of the handshaking region. They defined the kinetic and strain energy for the entire system including the handshaking region. Two different description of the material are envisioned, as shown in Figure 11, sitting on either side of the interface: in one case it is FE silicon and in the other it is MD silicon. The handshaking interactions at   SX0280

the interface to the first order can be approximated by means of two descriptions. More precisely, the handshaking potential is given by

$$V_{\text{FE/MD}} = \frac{1}{4} \sum_{m \in \tau_c} \sum_{p,q=1}^{p_{\max}} u_p^m K_{pq}^m u_q^m$$
$$+ \frac{1}{2} \sum_{(i<j) \in \beta_{2c}} V^{(2)}(\boldsymbol{r}_{ij})$$
$$+ \sum_{(i,(j<k)) \in \beta_{3c}} V^{(3)}(\boldsymbol{r}_{ij}, \boldsymbol{r}_{ik}) \quad (19)$$

where τ_c is the set of FE elements that cross the FE/MD interface, β_{2c} and β_{3c} are the sets of two-body and three-body bonds, respectively, that cross. Indeed, $V_{\text{FE/MD}}$ is only defined for interactions that cross the boundary. The other terms in Equations (17) and (18) define the forces at atomic and continuum region, respectively. The formalism in the above equation is meant to imply that any one atom of the triplet in the three-body terms can be on an opposite side of the interface to the other two.

SX0285   It is necessary to refine the FE mesh in the FE/MD handshaking region to coincide with the perfect atomic lattice. In this limit the kinetic energy is localized to the nodes since that is where the atoms are situated. Thus, for the FE region, the "lumped mass" approximation was used. One third of the mass in each 2D triangular element, and one fourth of the mass in each 3D tetrahedron, are apportioned to each apex in silicon. The kinetic energy is thus given by

$$K_{\text{FE}} = \sum_{a=1}^{N_{\text{mesh}}} \frac{1}{2} M_a |\dot{\boldsymbol{u}}_a|^2 \quad (20)$$

where a labels the FE mesh points, of which there are N_{mesh} total, and

$$M_a = \begin{cases} \rho \sum_{m=1}^{N_{\text{elem}}} \sum_{l=1}^{3} \delta_{a,m_l} V_m/3 & \text{in 2D} \\ \rho \sum_{m=1}^{N_{\text{elem}}} \sum_{l=1}^{4} \delta_{a,m_l} V_m/4 & \text{in 3D} \end{cases} \quad (21)$$

where m_l labels the mesh point index at each of the apexes of element m. The total number of FE elements is N_{elem}.

SX0290   Effectively, the FE algorithm involves an average over the atomic degrees of freedom that are missing from the mesh. Thus, to bring the atomic and continuum thermal energies onto an equivalent footing, the total FE thermal energy must be offset. These corrected energies are denoted by a prime:

$$K'_{\text{FE}} = \tfrac{3}{2}\Delta N k_{\text{B}} T + K_{\text{FE}} + \tfrac{1}{2}\delta N_{\text{mesh}} k_{\text{B}} T \quad (22)$$

$$V'_{\text{FE}} = \tfrac{3}{2}\Delta N k_{\text{B}} T + V_{\text{FE}} + \tfrac{1}{2}\delta N_{\text{mesh}} k_{\text{B}} T \quad (23)$$

where $\Delta N = N_{\text{atom}} - N_{\text{mesh}}$ and δ is 0 or 1 for 3D or 2D FE, respectively. N_{atom} is the number of atoms contained within an equivalent 3D volume, and k_{B} is the Boltzmann constant. Equipartition has been invoked, and fluctuations about the average energy are neglected in this expression. It is further assumed that the background temperature is constant during the simulation. The first term, therefore, accounts for the missing degrees of atomic freedom while the last term augments the 2D FE plane-strain simulation for the missing third dimension in its degrees of freedom. These offsets do not affect the dynamics of the system and the thermal corrections can be apportioned to each mesh point as described above for the zero temperature FE potential energy. For finite temperature simulations, the $\dot{\boldsymbol{u}}_a$ degrees of freedom are thermalized to a Maxwellian distribution. Also, the appropriate elastic constants for that temperature should be used in the FE equations of motion so as to make the MD and FE regions seamless and compatible. Further, since this methodology requires a continuation of ideal lattice sites into the FE/MD handshaking region in order to determine mesh coordinates, the appropriate lattice parameter for given temperature should be used.

(ii) Validation

Figure 12 shows the coupled FE/MD simu-   SX0295 lation on rapid brittle fracture of a silicon slab flawed by a microcrack at its center and under uniaxial tension. The waves pass through the MD/FE coupling interface with no visible reflection.

A hybrid MD/FE simulation can be com-   SX0300 pared with a large-scale pure MD result. Lidorikis *et al.* (2001) demonstrated a detailed comparison between hybrid simulation results and full MD multimillion-atom simulations in the study on stress distributions in silicon/silicon-nitride nanopixels. The hybrid approach provides atomistic description near the interface and continuum description deep into the substrate, increasing the accessible length scales and greatly reducing the computational cost. The results of the hybrid simulation are in good agreement with full multimillion-atom MD simulations: atomic structures at the lattice-mismatched interface between amorphous silicon nitride and silicon induce inhomogeneous stress patterns in the substrate that cannot be reproduced by a continuum approach alone.

8.12.4.2.2 *FEM/MD overlapping belt*

FE/MD coupling based on one-to-one dis-   SX0305 placement connection causes artificial blocking
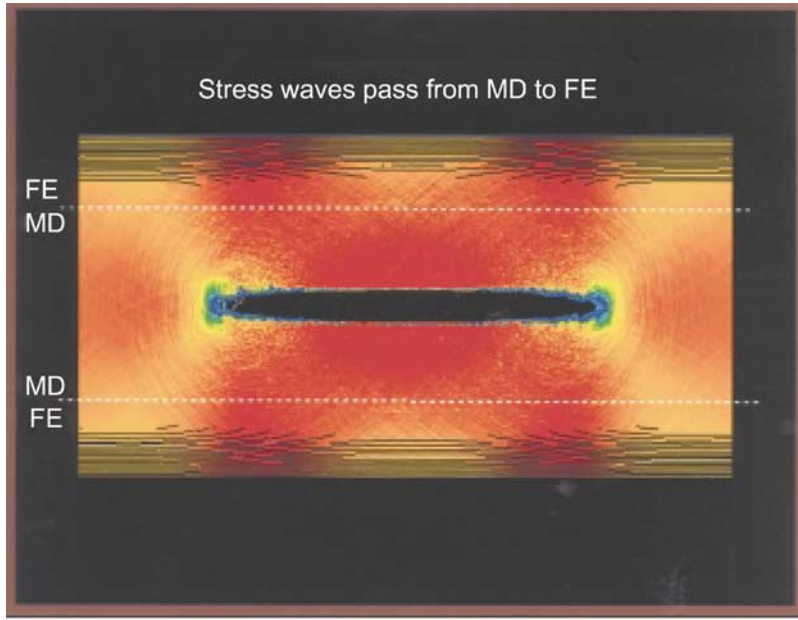
Figure 12 Elastic energy waves propagating through the slab, visualized using a potential-energy color scale (after Abraham *et al.*, 2000).

against dislocation transition. Tan and Yang (1994b) and Yang and Tan (1996) developed a more flexible combined continuum and atomistic simulation method to simulate fracture process. At the crack tip, the innermost continuum elements overlap the border rings of the atom aggregate by three to four interatomic distances. The overlapping area is denoted as L, continuum area as C, and atomic area as A. In region L, each FE node is surrounded by a group of atoms. A matrix $T_{L \leftarrow A}^u$ is introduced to convey the displacement from the atomic group to the corresponding FE node, and $T_{A \leftarrow L}^f$ for the force from FE node to the associated atoms. Thus, the transmission from atomistic description to continuum description in the overlapping layer for the displacement, velocity, and force can be expressed, respectively, as

$$\boldsymbol{u}_L = T_{L \leftarrow A}^u \boldsymbol{u}_A$$

$$\dot{\boldsymbol{u}}_L = T_{L \leftarrow A}^u \dot{\boldsymbol{u}}_A \tag{24}$$

$$\boldsymbol{f}_A = T_{A \leftarrow L}^f \boldsymbol{f}_L$$

The system potential energy is a functional of displacements in continuum, overlapping layer, and atom aggregate, that are $\boldsymbol{u}_C(t)$, $\boldsymbol{u}_L(t)$, and $\boldsymbol{u}_A(t)$, respectively

$$\Pi[\boldsymbol{u}_C(t), \boldsymbol{u}_L(t), \boldsymbol{u}_A(t)]$$
$$= \frac{1}{2} \begin{pmatrix} \boldsymbol{u}_C^{\mathrm{T}} & \boldsymbol{u}_L^{\mathrm{T}} \end{pmatrix} \begin{pmatrix} \boldsymbol{K}_{CC} & \boldsymbol{K}_{CL} \\ \boldsymbol{K}_{LC} & \boldsymbol{K}_{LL} \end{pmatrix} \begin{pmatrix} \boldsymbol{u}_C \\ \boldsymbol{u}_L \end{pmatrix}$$
$$- \begin{pmatrix} \boldsymbol{u}_C^{\mathrm{T}} & \boldsymbol{u}_L^{\mathrm{T}} \end{pmatrix} \begin{pmatrix} \boldsymbol{f}_C \\ \boldsymbol{f}_L \end{pmatrix} + \sum_{i \in A} E_i(\boldsymbol{u}_A) \tag{25}$$

where $\boldsymbol{K}_{CC}$, $\boldsymbol{K}_{CL}$, $\boldsymbol{K}_{LC}$, and $\boldsymbol{K}_{LL}$ are standard FE stiffness matrices, E_i is the embed energy of atom i.

The kinetic energy of the system is

$$T[\boldsymbol{u}_C(t), \boldsymbol{u}_L(t), \boldsymbol{u}_A(t)]$$
$$= \frac{1}{2} \begin{pmatrix} \dot{\boldsymbol{u}}_C^{\mathrm{T}} & \dot{\boldsymbol{u}}_L^{\mathrm{T}} \end{pmatrix} \begin{pmatrix} \boldsymbol{M}_{CC} & \boldsymbol{M}_{CL} \\ \boldsymbol{M}_{LC} & \boldsymbol{M}_{LL} \end{pmatrix} \begin{pmatrix} \dot{\boldsymbol{u}}_C \\ \dot{\boldsymbol{u}}_L \end{pmatrix}$$
$$+ \frac{1}{2} \dot{\boldsymbol{u}}_A^T \boldsymbol{M}_A \dot{\boldsymbol{u}}_A \tag{26}$$

where $\boldsymbol{M}_{CC}$, $\boldsymbol{M}_{CL}$, $\boldsymbol{M}_{LC}$, and $\boldsymbol{M}_{LL}$ are standard FE mass matrices, and $\boldsymbol{M}_A$ is the mass matrix of the atom aggregate that can be expressed as

$$\boldsymbol{M}_A = \begin{pmatrix} m_1 & & \boldsymbol{0} \\ & \ddots & \\ \boldsymbol{0} & & m_n \end{pmatrix}_{n \times n} \tag{27}$$

where m_i $(i = 1, \ldots, n)$ is the mass of atom I and n is the total number of atoms.

The Hamiltonian of the system is

$$H[\boldsymbol{u}_C(t), \boldsymbol{u}_L(t), \boldsymbol{u}_A(t)] = \int_{t_1}^{t_2} [T[\boldsymbol{u}_C(t), \boldsymbol{u}_L(t), \boldsymbol{u}_A(t)]$$
$$- \Pi[\boldsymbol{u}_C(t), \boldsymbol{u}_L(t), \boldsymbol{u}_A(t)]]\mathrm{d}t \tag{28}$$

According to the Hamiltonian's principle, the Hamiltonian of the displacement fields should be stationary under actual motions $\boldsymbol{u}_C(t)$, $\boldsymbol{u}_L(t)$, $\boldsymbol{u}_A(t)$, i.e.,

$$\delta H[\boldsymbol{u}_C(t), \boldsymbol{u}_L(t), \boldsymbol{u}_A(t)] = 0 \tag{29}$$

In the above equation, all virtual displacements satisfying (i) boundary conditions, (ii) initial and terminal conditions at t_1 and t_2, respectively, and (iii) the atomistic–continuum correspondence

$$\boldsymbol{u}_L(t) = T^u_{L \leftarrow A} \boldsymbol{u}_A(t)$$
$$\dot{\boldsymbol{u}}_L(t) = T^u_{L \leftarrow A} \dot{\boldsymbol{u}}_A(t) \qquad (30)$$

should be satisfied.

SX0325   The modified Hamiltonian functional is introduced to include the atomistic–continuum correspondence constraints (iii) into the Hamiltonian in Equation (28), and can be expressed as

$$H^*[\boldsymbol{u}_C(t), \boldsymbol{u}_L(t), \boldsymbol{u}_A(t), \lambda_L(t), \mu_L(t)]$$
$$= H[\boldsymbol{u}_C(t), \boldsymbol{u}_L(t), \boldsymbol{u}_A(t)]$$
$$+ \int_{t_1}^{t_2} \Big\{ \big[\boldsymbol{u}_L(t) - T^u_{L \leftarrow A} \boldsymbol{u}_A(t)\big]^{\mathrm{T}} \cdot \lambda_L(t)$$
$$+ \big[\dot{\boldsymbol{u}}_L(t) - T^u_{L \leftarrow A} \dot{\boldsymbol{u}}_A(t)\big]^{\mathrm{T}} \cdot \mu_L(t) \Big\} \mathrm{d}t \qquad (31)$$

By variational principle, among all the available displacements satisfying the above constraints (i) and (ii), the first variation of the modified Hamiltonian functional would vanish by the actual displacements

$$\delta H^*[\boldsymbol{u}_C(t), \boldsymbol{u}_L(t), \boldsymbol{u}_A(t), \lambda_L(t), \mu_L(t)] = 0 \quad (32)$$

SX0330   The governing equations of the atom aggregate can be obtained through straightforward algebra and expressed by

$$(\boldsymbol{M}_A + \hat{\boldsymbol{M}}_A)\ddot{\boldsymbol{u}}_A = \boldsymbol{f}(\boldsymbol{u}_A) + \hat{\boldsymbol{F}}_A + \hat{\boldsymbol{P}}_A - \hat{\boldsymbol{K}}_{AA}\boldsymbol{u}_A \qquad (33)$$

where $\hat{\boldsymbol{F}}_A$, $\hat{\boldsymbol{K}}_{AA}$, and $\hat{\boldsymbol{P}}_A$ are the forces, elastic constraints, and the D'Alembert inertia forces of the continuum acting on the atoms in the overlapping belt, and the matrix $\hat{\boldsymbol{M}}_A$ denotes the additional mass adhered to the overlapping atoms. They can be expressed as

$$\hat{\boldsymbol{F}}_A = T^f_{A \leftarrow L}(\boldsymbol{f}_L - \boldsymbol{K}_{LC}\boldsymbol{K}_{CC}^{-1}\boldsymbol{f}_C) \qquad (34)$$

$$\hat{\boldsymbol{K}}_{AA} = T^f_{A \leftarrow L}(\boldsymbol{K}_{LL} - \boldsymbol{K}_{LC}\boldsymbol{K}_{CC}^{-1}\boldsymbol{K}_{CL})T^u_{L \leftarrow A} \qquad (35)$$

$$\hat{\boldsymbol{P}}_A = T^f_{A \leftarrow L}(\boldsymbol{K}_{LC}\boldsymbol{K}_{CC}^{-1}\boldsymbol{M}_{CC} - \boldsymbol{M}_{LC})\ddot{\boldsymbol{u}}_C \qquad (36)$$

$$\hat{\boldsymbol{M}}_A = T^f_{A \leftarrow L}(\boldsymbol{M}_{LL} - \boldsymbol{K}_{LC}\boldsymbol{K}_{CC}^{-1}\boldsymbol{M}_{CL})T^u_{L \leftarrow A} \qquad (37)$$

Equation (33) allows the updating of atom locations with the interaction of overlapping continuum.

8.12.4.2.3 Multiscale defect propagation

Yang *et al.* (1994), Tan and Yang (1994b), and Yang and Tan (1996) simulated the transmission of crack-tip dislocations from the atomistic assembly to the overlapping continuum. Initially an interfacial crack is located on a zigzag interface. Different modes of loading are applied to examine the dislocation behavior. In atom assembly, no dislocation nucleation criterion is required. Atoms move under the interatomic potential described for the system. When an atomistic dislocation moves to the continuum region, it will be substituted *in situ* by a dislocation of the same Burgers vector but embedded in the FE-described continuum. As the consequence of the newly created continuum dislocation, the extra half-plane of atoms in the atomistic assembly is removed from the MD calculation to retain the global conversation of mass. In the continuum region, dislocation motion is directed by the crystal slip system with speed given by the dislocation dynamics curve. A singularity exclusion scheme is used to remove the strong singularity associated with dislocation self-stress fields and to achieve numerical efficiency (Zhang and Yang, 1994). Accordingly, the stress and deformation fields associated with a dislocation embedded in an otherwise infinite elastic continuum are evaluated analytically and subtracted from the overall field, and the complementary nonsingular fields due to the traction difference between the actual exterior boundary condition and the negating forces for dislocation self-stress can be solved by the FE.   SX0335   SX0340

The simulation shown in Figure 13 demonstrates the multiscale dislocation propagation. The atomistic dislocations nucleated from the crack tip can penetrate the atom-continuum overlapping layer by a technique that converts the lattice defects (atomistic dislocations) to the discrete singularities (continuum dislocations). The velocity vs. crack-tip distance curve indicates that the propagation of the dislocation from the atom assembly to the surrounding continuum is continuous. The dislocation velocities predicted by MD simulations agree well with the phenomenological dislocation dynamics curve.   SX0345

Noguchi and Furuya (1997) proposed a method that combines a crack-tip MD enclave with a linear elastic outer domain in simulating elastic-plastic crack advance. An MD model was applied to the crack-tip region and a micromechanics model to the surrounding region. In this mixed model, however, crack propagation simulation must be stopped when the crack tip reaches the boundary of the two   SX0350
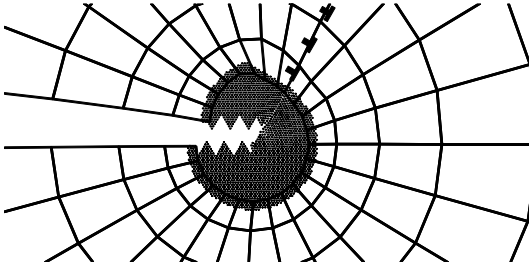
Figure 13 Combined MD/dislocation/FE simulation interfacial fracture. The model consists of a nanoscopic core made by atomistic assembly and a surrounding elastic continuum with discrete dislocations. Atomistic dislocations nucleated from the crack tip and move to the continuum layer where they glide according to the dislocation dynamics curve. An atoms/continuum overlapping belt is devised to facilitate the transition between the two scales. The effect of atomistic zigzag interface on the fracture process is revealed: it hinders dislocation emission from the crack tip, especially under high mode mixity.

regions. The method can be improved by moving the MD region successively with crack propagation (Furuya and Noguchi, 1998). Furuya and Noguchi (2001) and Furuya *et al.* (2001) simulated the crack propagation and brittle fracture with a combined model of MD with micromechanics. The critical stress intensity factor for dislocation emissions was discussed to investigate the thermal effect on the brittle fracture processes.

8.12.4.3 Quasicontinuum Method

Ortiz and Phillips (1999) reviewed quasicontinuum (QC) theory of Tadmor *et al.* (1996a, 1996b). The method is becoming mature for multiscale simulations, Ortiz *et al.* (2001). The QC theory starts from an underlying conventional atomistic model and strives to systematically eliminate redundant degrees of freedom. In this method, interatomic interactions are incorporated in the model via the discrete lattice calculation based on the local state of deformation. Shenoy *et al.* (1999) reformulated this model to examine the interactions between grain boundaries, dislocations, and cracks. The QC method differs from FEM in that the constitutive input is drawn directly from calculations at the atomic scale. The QC method links atomistic and continuum models through the device of the FE method that permits a reduction of the full set of atomistic degrees of freedom. They tie the need for automatic adaptation to an estimate of the error introduced by the reduction of the degrees of freedom. It is then possible to identify regions where the error estimator is

high, and subsequently to add degrees of freedom in these regions. Based on lattice statics, however, the QC method is a non-dynamical formalism that brings atomic information into the continuum mechanics of deformation. Currently, the QC method is limited to static energy minimization.

Knap and Ortiz (2001) presented a streamlined and fully 3D version of the QC theory and analyzed its accuracy and convergence characteristics. Consider a crystal whose N atoms occupy a subset of a Bravais lattice

$$X(l) = \sum_i l^i a_i, \quad l \in L \subset Z^d \qquad (38)$$

where $d \le 3$ is the dimension of the lattice. The coordinates of the atoms in a deformed configuration of the crystal are $\{x(l), l \in L\}$. Collect all atomic coordinates in an array x and regard such array as an element of the linear space $X \equiv R^{Nd}$, the "configuration" space of the crystal.

On loading the solid, the equilibrium configuration of the body is defined by the set of displacements u_i that minimizes the potential function

$$\Pi(u) = E_{\text{tot}}(u_1, \ldots, u_N) - \sum_{i=1}^{N} f_i \cdot u_i \qquad (39)$$

where E_{tot} is the total energy of the system obtained from an atomistic formulation, f_i is the external force acting on the atom I, and u satisfies essential boundary conditions of the problem. It is assumed that E_{tot} can be decomposed as a sum over the energies of individual atoms E_i, i.e.,

$$E_{\text{tot}}(u_1, \ldots, u_N) = \sum_{i=1}^{N} E_i(u_1, \ldots, u_N) \qquad (40)$$

The spirit of the problem is now identical to that of numerical quadrature, and what is required at this point is a scheme for approximating the sum given above by summing over the representative atoms with appropriate weights selected so as to account for differences in element size and environment. In particular,

$$E_{\text{tot}} \approx \sum_{\alpha=1}^{R} n_\alpha E_\alpha \qquad (41)$$

The crucial idea embodied in this equation surrounds the selection of some set of representative atoms, each of which is intended to characterize the energetics of some spatial neighborhood within the body as indicated by the weight n_α. Physically the quantity n_α may be interpreted as the "number of atoms

represented" by the representative atom α. The problem is

$$\min_{u} \Pi(u) \qquad (42)$$

8.12.4.3.1 Interpolation

SX0380   The essence of the theory of Tadmor *et al.* (1996a, 1996b) is to replace Equation (42) by a constrained minimization of $\Pi(u)$ over a suitably chosen subspace X_h of X. In order to define X_h, one begins by selecting a reduced set $L_h \subset L$ of $N_h < N$ representative atoms (Figure 14). The selection of the representative atoms is based on the local variation of the fields. In addition, introduce a triangulation T_h of L_h. It bears emphasis that the triangulation T_h may be unstructured. In particular, L_h need not define a Bravais lattice. The positions of the remaining atoms are determined by piecewise linear interpolation of the representative atom coordinates. One should regard the resulting coordinates $\{x_h(l), l \in L_h\}$ as belonging to a linear space X_h of dimension $N_h d$.

SX0385   Let $\varphi(X|l_h)$, $l_h \in L_h$, be a collection of shape functions for T_h. Thus, $\varphi(X|l_h)$ is continuous and piecewise linear, its domain is restricted to the simplexes of T_h incident to $X(l_h)$, and it vanishes at all nodes of the triangulation except at $X(l_h)$, where it takes the value 1, i.e.,

$$\varphi(X(l'_h)|l_h) = \delta(l'_h|l_h) \qquad (43)$$

By construction,

$$x_h(l) = \sum_{l_h \in L_h} \varphi_h(l|l_h) x(l_h) \qquad (44)$$
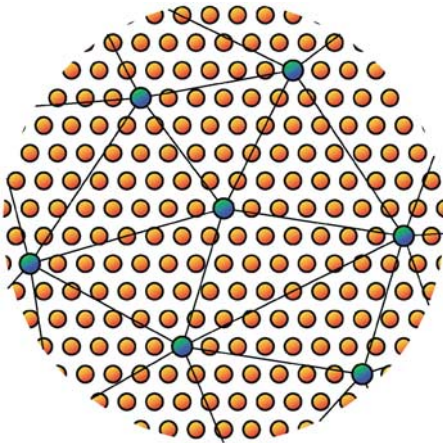
where one writes

$$\varphi_h(l|l_h) = \varphi_h(X(l)|l_h) \qquad (45)$$

Figure 14 Example of triangulation T_h of the crystal (after Knap and Ortiz, 2001).

Evidently, $\{\varphi_h(l|l_h), l_h \in L_h\}$ constitutes a basis   SX0390
for X_h and the fields $x_h(l)$ are entirely determined by their values $x_h(l_h)$ at the representative atoms. In addition, the basis lattice functions are required to satisfy the identity:

$$\sum_{l_h \in L_h} \varphi_h(l|l_h) = 1 \qquad (46)$$

i.e., the basis lattice functions must be a partition of unity over L. This requirement ensures that constant fields are interpolated exactly by the basis lattice functions.

8.12.4.3.2 Reduced equations

The reduced counterpart of problem Equa-   SX0395
tion (42) is now

$$\min_{u_h \in X_h} \Pi(u_h) \qquad (47)$$

The minimizers of the reduced problem satisfy the reduced equations of equilibrium

$$\bar{f}_h(l_h) = \sum_{l \in L} f(l|x_h) \varphi_h(l|l_h) = 0 \qquad (48)$$

Here,

$$f_h(x) = \Pi_{,x}(x) \qquad (49)$$

are the forces corresponding to x and $f(l|x_h)$ is the value of $f(x)$ at site l. Thus, the reduced problem entails the solution of $N_h d$ unknowns $x(l_h)$, $l_h \in L_h$, from Equation (48) of the same order.

8.12.4.3.3 Application: interactions between cracks and grain boundaries

Using QC simulations, Miller *et al.* (1998a)   SX0400
studied the problem of interactions between cracks and grain boundaries. Mechanistic understanding of the role of grain boundaries in fracture of polygranular materials requires a correct atomic-level description of both the advancing crack tip, and the structure of the grain boundary itself. The QC formulation was extended to treat polycrystals by Shenoy *et al.* (1998). In the same work it was demonstrated that the method predicts grain boundary structures in excellent agreement with fully atomistic models. Miller *et al.* (1998b) coupled the accurate modeling of grain boundary structure with the ability to model fracture processes demonstrated in the previous section. This is a problem whose size scale is well suited to the QC method, as multiple length scales are clearly at work. These length scales range from those needed to capture the elastic differences

between the two grains to the detailed atomistic mechanisms of fracture, dislocation generation, and grain boundary migration.

SX0405   In Figure 15, the nickel bicrystal considered contains a $\Sigma21(421)$ symmetric tilt boundary, which has a $[11\bar{2}]$ tilt axis and a tilt angle of 44.41°. A crack is initiated in the model by removing a single (111) plane from one of the grains. The crystallography of this grain boundary dictates that such a (111) plane is oriented at an angle of 67.8° to the grain boundary. The two crystals are oriented such that the crack plane lies on the *x*-axis and the grain boundary extends obliquely through the model. The initial mesh is shown in Figure 15, with a close-up of the fully refined crack-tip region in the inset.

SX0410   The QC technique has been applied to defective systems (such as cracks, dislocations, and interfaces) in both 2D and 3D, where the defects are treated in an atomistic region embedded in a continuum. This approach has the advantage that it avoids the usual assumptions inherent in continuum models, such as the rather *ad hoc* criterion typically used for failure in a given region of space. It also allows for slip within the FE. The QC technique has also been used to study nanoindentation (Shenoy *et al.*, 2000; Smith *et al.,* 2001). Qian *et al.* (2002) extended the QC method to the analysis of the nanotube system with some treatments because nanotube is composed of atomic layers.

8.12.4.4   Coarse-grained Molecular Dynamics

Rudd and Broughton (1998) developed   SX0415 coarse-grained molecular dynamics (CGMD). In this approach, the continuum-level (or coarse-grained (CG)) energy is given by an ensemble average over the atomic motions in which the atomic positions are constrained to give the proper coarse-scale field. In this way, the fine scale quantities that are not included in the coarse scale motion are not neglected completely, as their thermodynamic average effect is retained.

CGMD is a substitute for FE that connects   SX0420 to MD in the atomic limit. It also reproduces the results of FE, with slight improvements, in
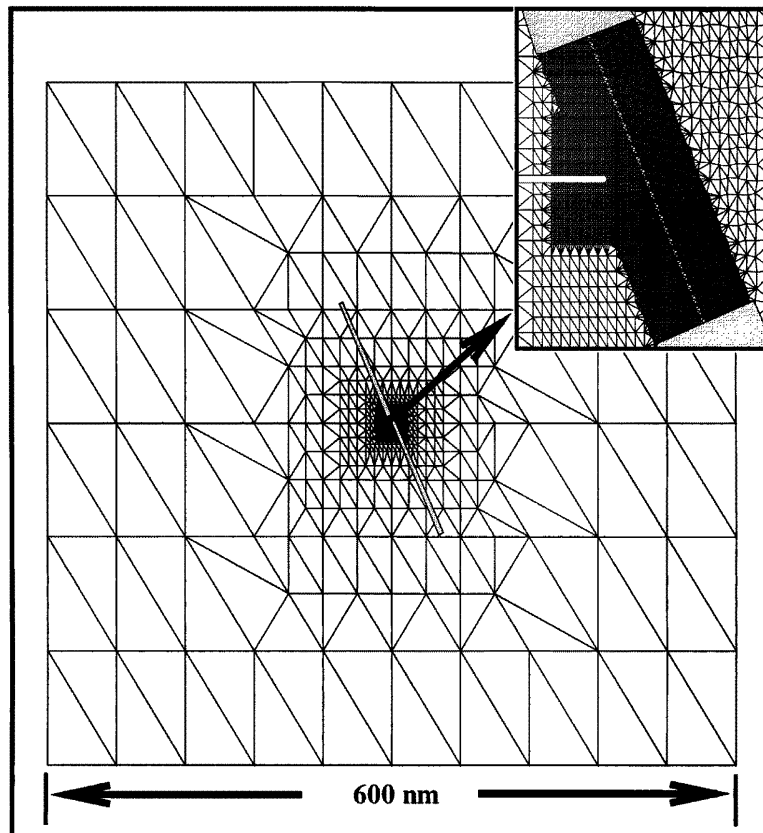

Figure 15 Mesh used in the QC model of the interaction between a crack and a grain boundary. Approximate dimension is shown, and the inset shows a close-up of the fully refined region near the crack tip. The regions in the mesh where adaptation is not allowed to take place are shown schematically by the shaded gray boxes (after Miller *et al.*, 1998b).

large element size. The method provides spatially optimized algorithms based on statistical mechanical coarse-graining procedures. The equations of motion in the formalism are similar in flavor to FE, but they do not rely on the assumptions of continuum elastic theory. The constitutive equations used in FE are modified in an element-size-dependent fashion. The MD equations of motion are recovered in the atomistic limit, and those of continuum elastic theory in the bulk in the macroscopic limit. Thus, a single simulation has MD regions running concurrently and seamlessly with improved FE regions much larger in size. This is ideal for the study of mesoscopic elastic solids.

SX0425	Given a microscopic potential energy expression describing the motion of atoms in a solid, crystalline or amorphous, and a CG mesh partitioning the solid into elements. The mesh size may vary, so that in important regions a mesh node is assigned to each equilibrium atomic position, whereas in other regions the elements contain many atoms and the nodes need not coincide with atomic sites. CGMD produces equations of motion for a mean displacement field defined at the nodes. In particular, the conserved energy functional for the CG system is a constrained ensemble average of the atomistic energy under fixed thermodynamic conditions. The equations of motion are Hamilton's equations for this energy functional.

SX0426	The classical ensemble must obey the constraint that the position and momenta of the atoms are consistent with the mean displacement and momentum fields. Let the displacement of atom μ be $\boldsymbol{u}_\mu = \boldsymbol{x}_\mu - \boldsymbol{x}_{\mu 0}$, where $\boldsymbol{x}_{\mu 0}$ is its equilibrium position. The displacement of mesh node j is an average of the atomic displacements

$$\boldsymbol{u}_j = \sum_\mu f_{j\mu} \boldsymbol{u}_\mu \qquad (50)$$

where $f_{j\mu}$ is a weighting function, related to the microscopic analogy of FE interpolating function. An analogous relation is implied for the momenta $\boldsymbol{p}_u$. Since the nodal displacements are fewer or equal to the atomic positions in number, fixing the nodal displacements and momenta does not necessarily determine the atomic coordinates. Some subspace of phase space remains, corresponding to degrees of freedom that are missing from the mesh. The CG energy is defined as the average energy of the canonical ensemble on this constrained phase space,

$$E(\boldsymbol{u}_k, \dot{\boldsymbol{u}}_k) = \int \mathrm{d}x_\mu \, \mathrm{d}p_\mu \, H_{\mathrm{MD}} e^{-\beta H_{\mathrm{MD}}} \Delta / Z \quad (51)$$

where $\beta = 1/kT$ is the inverse temperature, Z is the partition function and

$$\Delta = \prod_j \left[\delta\left(\boldsymbol{u}_j - \sum_\mu \boldsymbol{u}_\mu f_{j\mu}\right) \cdot \delta\left(\dot{\boldsymbol{u}}_j - \sum_\mu \frac{\boldsymbol{p}_\mu}{m_\mu} f_{j\mu}\right) \right] \tag{52}$$

where $\delta(\boldsymbol{u})$ is a 3D delta function. The delta function enforces the mean field constraint. Note that Latin indices, j, k,..., denote mesh nodes and Greek indices, μ, v,..., denote atoms. The energy is computed as follows.

SX0430	When the mesh nodes and the atomic sites are identical, the CGMD equations of motion agree with the atomistic equations of motion. As the mesh size increases some short wavelength degrees of freedom are not supported by the coarse mesh. These degrees of freedom are not neglected entirely, because their thermodynamic average effect has been retained. The CG energy may be computed using standard techniques. The atomistic Hamiltonian is

$$H_{\mathrm{MD}} = \sum_\mu \frac{\boldsymbol{p}_\mu^2}{2m} + \sum_{\mu,v} \boldsymbol{u}_\mu \cdot D_{\mu v} \cdot \boldsymbol{u}_v \qquad (53)$$

where $D_{\mu v}$ is the dynamical matrix. It acts as a tensor on the components of the displacement vector at each site. Define the mass matrix by the matrix inverse

$$M_{jk} = m \left(\sum_\mu f_{j\mu} f_{k\mu} \right)^{-1} \qquad (54)$$

and the stiffness matrix in a similar way

$$K_{jk} = m \left(\sum_{\mu,v} f_{j\mu} D_{\mu v}^{-1} f_{k\mu} \right)^{-1} \qquad (55)$$

SX0435	The CG energy for a monatomic harmonic solid of N atoms CG to N_{node} nodes is computed to be

$$E(\boldsymbol{u}, \dot{\boldsymbol{u}}_k) = U_{\mathrm{int}} + \sum_{j,k} \left(\dot{\boldsymbol{u}}_j \cdot M_{jk} \dot{\boldsymbol{u}}_k + \boldsymbol{u}_j \cdot K_{jk} \cdot \boldsymbol{u}_k \right) \quad (56)$$

where $U_{\mathrm{int}} = 3(N - N_{\mathrm{node}})kT$. The energy contains terms representing the average kinetic and potential energies, plus the thermal energy term expected from the equipartition theorem for the modes that have been integrated out. This Hamiltonian is generalized easily to polyatomic solids, where the optical modes may be CG in several ways to represent different physics.

SX0440	The stiffness matrix K_{ij} is to be computed at the start of a simulation, and it remains unaltered during the subsequent dynamics. It

does not matter whether atoms vibrate across element boundaries, as long as diffusion is negligible. An efficient computation of K_{ij} is achieved through a normal mode decomposition of D_{mn}. Use of Bloch symmetry reduces the size of the dynamical matrix to be inverted to the size of the superelement of which the system is comprised. Note that for $T \neq 0$ the finite temperature dynamical matrix should be used for D_{mn}. This ensures consistent thermodynamics. e.g., in ergodic systems the time average of the kinetic energy term in the CG energy is related to the temperature. In general, the dynamical matrix may depend on other macroscopic parameters, as well, such as slowly varying external magnetic and electric fields. D_{mn} should be evaluated under these conditions. Also note that while the harmonic approximation may be good in peripheral regions, it may not be appropriate for the important regions.

SX0445   The CGMD and MD equations of motion agree in regions where the mesh coincides with the atomic sites. In these regions, the full MD potential is restored, so that effects such as diffusion and dislocation are allowed.

SX0450   1D chains of atoms with periodic boundary conditions are considered for validation of the method. Figure 16 shows the phonon spectrum for atoms with harmonic interactions CG to a regular, but not necessarily commensurate mesh. The normal modes are plane waves both on the underlying ring of atoms and on the CG mesh. The wave vector $\boldsymbol{k}$ is a good quantum number for both. The nonzero terms of the dynamical matrix are of the form: $D_{\mu\mu} = 2K$ and $D_{\mu,\mu\pm1} = -K$.

Figure 16 shows that CGMD gives a better approximation to the true phonon spectrum than two kinds of FE. All three do a good job at the longest wavelengths, as expected, but CGMD offers a higher order of accuracy. The relative error for CGMD is $O(k^4)$ while that of two versions of FE is only $O(k^2)$. At shorter wavelengths, there are significant deviations from the exact spectrum. The worst relative error of CGMD is $\sim 6\%$, three times better than that for FE. This improvement is made possible by the longer-ranged interactions of CGMD as compared to FE. The continuity condition satisfied by linear interpolation is enough to ensure that the hydrodynamic modes ($k \sim 0$) are well modeled, but the lack of continuity of the derivatives shows up as error in the spectrum of the modes away from the zone center. This error vanishes for the smooth, nonlocal basis consisting of the longest wavelength normal modes. It turns out that the CGMD error at the CG zone boundary is relatively small (less than 1%) for technical reasons. Also note that even though the number of atoms varies from element to element in the incommensurate mesh, the CGMD spectrum is free of anomalies. Other computations have shown that CGMD with linear interpolation is well-behaved on irregular meshes.

8.12.4.5   Lattice Material Point Method

    The basic idea of lattice material point method (LMPM) is that a continuum material point is also an aggregate of atoms. LMPM evolves from MD, an atomistic method, and
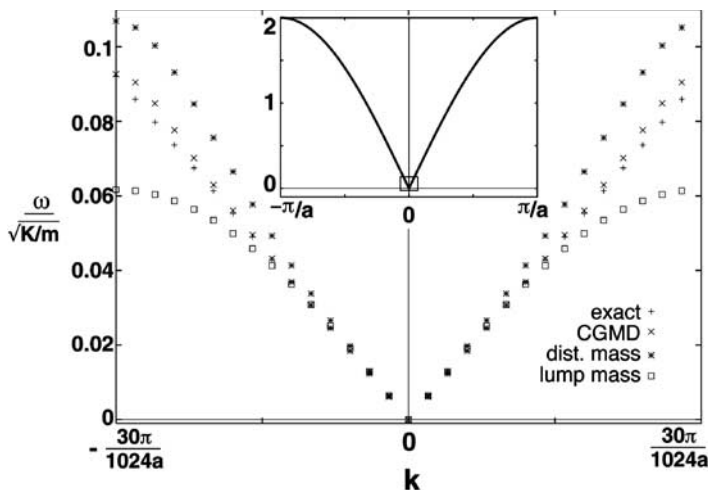
SX0455

SX0460

Figure 16 The phonon spectra shown result from various treatments of a ring of 1024 atoms and an incommensurate regular mesh of 30 nodes. The inset is the exact phonon spectrum, where the CG spectrum occupies the small box near the zone center. The error in the CGMD spectrum is much less than that of the FE spectra (after Rudd and Broughton, 1998).

material point method (MPM), a continuum method. The MD/MPM connection is realized by lattice material point (LMP) and the background grid.

8.12.4.5.1 *Material point method*

SX0465   MPM has evolved from an earlier method developed for fluid dynamics at the Los Alamos National Laboratories, called the particle-in-cell method. The MPM has been validated on such problems as elastic wave propagation (Sulsky *et al.*, 1994), the Taylor impact problem (Sulsky *et al.*, 1995; Sulsky and Schreyer, 1996), the upsetting problem (Sulsky and Schreyer, 1996), granular materials (Bardenhagen *et al.*, 2000), and contact problems (Bardenhagen *et al.*, 2000, 2001). Guilkey and Weiss (2002) developed and implemented an implicit integration strategy for MPM. As shown in Figure 17, MPM utilizes two representations of the continuum—one based on a collection of material points and the other based on a computational grid. In the method, the bulk material is discretized into a finite collection of material points. The material points are followed throughout the deformation of a solid and provide a Lagrangian description that is not subject to mesh tangling. Each material point is given an initial mass consistent with the material density and a volume of the point. Material parameters such as mass, displacement, velocity, stresses, strains, and temperature are assigned to each material point according to the material it represents. As the numerical solution proceeds, the material points are tracked and their states updated so that they carry the complete solution. To determine the motion of the
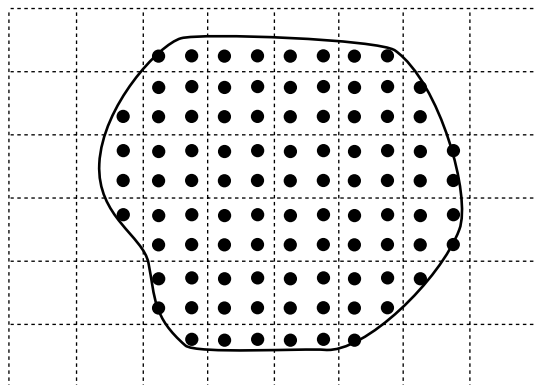
material points in an efficient manner, information from the material points is projected onto a background computational grid. The motion and temperature equations are solved on the grid. The solution on the grid is then used to update the position, velocity, and temperature of the material points. Velocity increments computed on the grid are interpolated to the material points to evaluate constitutive equations and update stress states for each material point.

MPM is chosen for continuum simulations   SX0470
that will be coupled with atomistic MD simulations for the following reasons: (i) MPM has the ability to handle large deformations in a more natural manner. Usually there is large deformation gradient at the atomic region. (ii) Parallel processing is more straightforward because of the use of a structured grid. (iii) Because of the particle description of the material, the method can be integrated with MD simulations, where material is handled as a collection of atoms (another kind of particles), in a unified way. (iv) The use of a background grid enables structured adaptive refinement. The MPM cell can adapt to different local resolution requirements by dividing into smaller cells. Dividing the time step in half successively as the cells get smaller can include time adaptivity. The computational grid is discarded once the material points have been updated and a new (undeformed) grid is defined to begin the next time step. As the new grid has no relation to the previous one, adaptive refinement based on the current solution is naturally available. This feature is of great benefit in interfacing MPM with MD simulations.

8.12.4.5.2 *MPM for mechanical systems*

Basic theory for MPM of the deformation of   SX0475
a solid system is described here.

(i) Governing equations and weak form

Newton's equations of motion for a solid material are

$$\sigma_{ij,j} + b_i = a_i \qquad (57)$$

where b_i is the force density, a_i is the acceleration, and σ_{ij} is the specific stress tensor defined as the regular stress tensor divided by the mass density ρ. The material constitutive equations can be represented as

$$\dot{\sigma}_{ij} = E_{ijkl} v_{k,l} \qquad (58)$$

where v_i is the velocity and E_{ijkl} is the specific elastic tensor defined as the regular elastic tensor divided by the mass density ρ.

Figure 17 A schematic view of a 2D MPM calculation. The solid line is an outline of the body analyzed. The black dots are the material points. The dashed lines here show a regular, background grid for calculation.

SX0480 The general equations in weak forms are

$$\int_{\partial\Omega} wT_i \, \mathrm{d}S + \int_\Omega \rho b_i w \, \mathrm{d}V$$
$$= \int_\Omega \rho a_i w \, \mathrm{d}V + \int_\Omega \rho \sigma_{ij} w_{,j} \, \mathrm{d}V \quad (59)$$

and

$$\int_\Omega \left(\dot{\sigma}_{ij} - E_{ijkl} v_{k,l} \right) \rho w \, \mathrm{d}V = 0 \quad (60)$$

where w is an arbitrary spatial function and boundary traction force

$$T_i = \rho \sigma_{ij} n_j \quad (61)$$

where n_j is the normal vector at the boundary surface. The solution of system Equations (59) and (60) need discretization of the domain and interpolation scheme to describe the field. MPM uses particles to isolate the domain into small material points. A background grid is used to describe the field and facilitate the interpolation.

(ii) Particle discretization

SX0485 The problem domain is divided into discrete small regions. Each small region $\Omega^{(p)}$ is called a particle, and given a label as particle p. The entire problem domain is $\bigcup_p \Omega^{(p)}$. The mass density can thus be approximated with a Dirac function

$$\rho(\boldsymbol{x}) = \sum_p m^{(p)} \delta \left[\boldsymbol{x} - \boldsymbol{x}^{(p)} \right] \quad (62)$$

where $m^{(p)}$ is the mass of particle p, which is

$$m^{(p)} = \int_{\Omega^{(p)}} \rho(x) \, \mathrm{d}V \quad (63)$$

Applying this approximation, one converts the weak form Equations (59) and (60) into each isolated particle as

$$\int_{\partial\Omega} wT_i \, \mathrm{d}V + \sum_p m^{(p)} b_i^{(p)} w^{(p)}$$
$$= \sum_p m^{(p)} a^{(p)} w^{(p)} + \sum_p m^{(p)} \sigma_{ij}^{(p)} w_{,j}^{(p)} \quad (64)$$

and

$$\dot{\sigma}_{ij}^{(p)} = E_{ijkl} v_{k,l}^{(p)} \quad (65)$$

respectively.

(iii) Interpolation

SX0490 Further conversion of the field Equation (64) into each isolated particle needs grid interpolation scheme

$$\phi(\boldsymbol{x}) = \sum_n \bar{\phi}^{(n)} N^{(n)}(\boldsymbol{x}) \quad (66)$$

where $\bar{\phi}^{(n)}$ is the grid value at node n. Here the bar symbol is used to denote the node value. The shape function between node n and particle p is denoted as $N^{(n,p)} = N^{(n)}[\boldsymbol{x}^{(p)}]$. Under this interpolation scheme, one can interpolate the particle value of arbitrary spatial function w, velocity $\boldsymbol{v}$, and acceleration $\boldsymbol{a}$ from the corresponding node values.

SX0495 Applying the interpolation scheme for acceleration to the weak form of Newton's Equation (64) gives

$$\sum_{n'} \bar{m}^{(n,n')} \bar{a}_i^{(n')} = \bar{F}_i^{(n)} + \bar{f}_i^{(n)} \quad (67)$$

where the external force on node n is

$$\bar{F}_i^{(n)} = \int_{\partial\Omega} N^{(n)} T_i \, \mathrm{d}V + \sum_p m^{(p)} b_i^{(p)} N^{(n,p)} \quad (68)$$

the internal force caused by stress gradient is

$$\bar{f}_i^{(n)} = -\sum_p m^{(p)} \sigma_{ij}^{(p)} N_{,j}^{(n,p)} \quad (69)$$

and the mass matrix between nodes n and n' is

$$\bar{m}^{(n,n')} = \sum_p m^{(p)} N^{(n,p)} N^{(n',p)} \quad (70)$$

(iv) Broken cell shape function

SX0500 Tan proposed the broken cell shape function for fracture simulation in MPM (CSAFE, 2000, 2001; Tan 2002). When a crack propagates and passes a particle, a particle variable (vector) named crack surface normal is associated to that particle. To handle explicit crack tracking in MPM, the particle–node visibility information is used to modify the normal shape functions used for field interpolations. In other words, a particle in a cell will not interpolate information to a grid node if a crack surface blocks the particle–node connection (Figure 18). The visibility connection between particle p and node n, $Vis^{(n,p)}$ is defined as

$$Vis^{(n,p)}$$
$$= \begin{cases} 1, & \text{particle } p \text{ can see node } n \\ 0, & \text{if particle } p \text{ is blocked from node} \\ & n \text{ by crack surface} \end{cases} \quad (71)$$

SX0505 The total number of the visible nodes to particle p is $S_{vis}^{(p)} = \sum_{n \in \text{nodes around } p} Vis^{(n,p)}$. The regular shape function between particle p and node n, $N^{(n,p)}$, is modified into broken cell
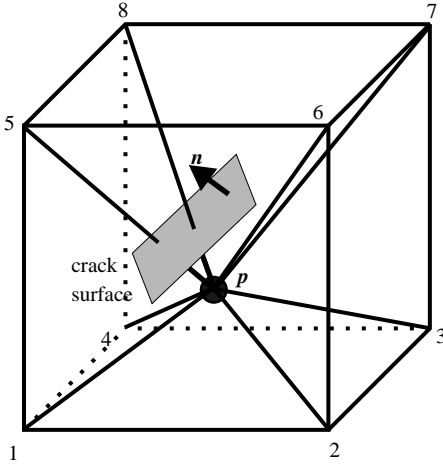
Figure 18 A crack surface can block the visibility of a cracked particle to a node at the other side of the crack. In the figure particle p loses direct interpolation relationship with node 5 and 8, because the visibility between particle p and node 5, 6 is blocked by the crack surface.

shape function, $\tilde{N}^{(n,p)}$, as

$$\tilde{N}^{(n,p)} = N^{(n,p)}$$
$$+ \frac{\sum_{m \in \text{nodes around } p} N^{(m,p)}\left[1 - Vis^{(m,p)}\right]}{S_{vis}^{(p)}} \quad (72)$$

This modified broken cell shape function satisfies the basic shape function requirements.

SX0510   The fracture simulation using broken cell shape function is demonstrated on a three-point bending problem. Our simulations are consistent with the theoretical predictions on the critical loading that causes fracture in the material (CSAFE, 2000). By analyzing the particle stress tensors computed via MPM, a determination is made where cracks would initiate and in what direction they should propagate. The crack initiation and propagation are simulated by creating a new micro-crack surface facet associated with a broken particle that will block the particle–node visibility, thus modifying the shape function and creating a numerical microcrack. In addition, in analyzing the crack-tip energy release rate, the simulation computes how much heat is transferred from mechanical strain energy around the crack tip zone.

8.12.4.5.3   MPM for thermal system

SX0515   To describe a thermal system, each material point has temperature $\theta^{(p)}$ and temperature gradient $\tau_i^{(p)}$. The interpolation from grid to particle gives

$$\theta^{(p)} = \sum_n \bar{\theta}^{(n)} N^{(n,p)} \quad (73)$$

and

$$\tau_i^{(p)} = \sum_n \bar{\theta}^{(n)} N_{,i}^{(n,p)} \quad (74)$$

where $\bar{\theta}^{(n)}$ is the temperature on node n. The mapping from particle to grid can be expressed by

$$\sum_p N^{(n,p)} M^{(p)} \theta^{(p)} = \bar{M}^{(n)} \bar{\theta}^{(n)} \quad (75)$$

where $\bar{M}^{(n)}$ is the lumped mass as node n and is defined as

$$\bar{M}^{(n)} = \sum_{n'} m^{(n,n')} \quad (76)$$

The heat conduction equations are solved on nodes as

$$cM^{(n)}\dot{\bar{\theta}}^{(n)} = \bar{H}^{(n)} + \bar{h}^{(n)} \quad (77)$$

where c is the thermal conductivity. The heat rate generated by heat sources can be expressed as

$$\bar{H}^{(n)} = \sum_p M^{(p)} N^{(n,p)} \frac{q^{(p)}}{\rho^{(p)}} \quad (78)$$

where $q^{(p)}$ is the heat source at particle p. The heat rate generated by heat flux is

$$\bar{h}^{(n)} = -\sum_p M^{(p)} \frac{k\tau_i^{(p)}}{\rho^{(p)}} N_{,i}^{(n,p)} \quad (79)$$

Figure 19 shows our simulation on crack tip   SX0520
temperature field. The crack was assumed to propagate when the dynamic energy release rate $G(t)$ was equal to the toughness of the material that was taken as $G_c = 100\,\text{J}\,\text{m}^{-2}$. In this simulation, G_c was assumed to be independent of crack velocity and 100% of the released energy was converted to heat. Another contribution to heat source is plastic work. Near a running crack tip, the plastic work rate is high. According to the theory of irreversible thermodynamics, the majority of the plastic work will be converted into heat that may lead to high temperature rise at the running crack tip. The plastic zone is regarded as the zone of heat source, and the plastic work rate as the strength of heat source. In the simulation, we assume that plastic work is transferred fully to heat.

8.12.4.5.4 *Adaptive material point method*

To refine material points adaptively during an MPM calculation, Tan and Nairn (2002) introduced a dimensionless refinement parameter at grid node n, $R_{\text{node}}^{(n)}$. Based on the gradient of a current grid calculation result of a field value $\phi(\boldsymbol{x})$, the refinement parameter is

$$R_{\text{node}}^{(n)} = \left| \frac{\langle \phi^{(\pm)} \rangle}{\phi^{(n)}} - 1 \right| \qquad (80)$$

where $\langle \phi^{(\pm)} \rangle$ is the average of $\phi(\boldsymbol{x})$ at the four neighboring nodes. In the adaptive MPM calculations, the value of $R_{\text{node}}^{(n)}$ at each grid node is evaluated for each time step. Then, for each cell in the calculation grid, we evaluate $R_{\text{cell}}^{(c)}$, which is the average value of $R_{\text{node}}^{(n)}$ from all nodes for that cell. If $R_{\text{cell}}^{(c)} > R_{\text{crit}}$, where R_{crit} is a predetermined critical value, each material point in that element was split into four points as shown in Figure 20. The adaptivity is hierarchical because at the next step the four new elements are examined individually and one or more may continue to refine. The refinement process is illustrated in Figure 20. In problems with crack propagation, it is possible to recombine material points when refinement is no longer needed. In other words, if $R_{\text{cell}}^{(c)} < R_{\text{crit}}$ for some previously refined elements, the material points can be recombined. Recombination should be straightforward for elastic materials but might require some approximations for history-dependent

materials. Finally, notice that after the second refinement in Figure 20 the upper-right and lower-left cells do not refine, but each has an extra mid-node in the sides connected with the refined cell. Thus the shape functions for upper-right and lower-left cells, generally expressed in Equation (66), should take account of these extra mid-nodes. Basically the adaptive-mesh shape functions accounted for such adaptive cells by allowing the n in Equation (66) to be 4–8 for a 2D grid.

We tested the adaptive MPM on a double cantilever beam (DCB) with energy release rate calculation. The material points and the initial unrefined, background grid are shown in Figure 21. The beam dimensions were 100 mm long with a square cross-section 10 mm × 10 mm. The crack length was 50 mm long or the crack tip was in the middle of the specimen. The load was applied at the end of the specimen. The displacements of the background grid nodes in the vertical direction were constrained to zero as indicated. The crack tip is at the left-most constrained node. This grid models only half the specimen; the other half is formed by symmetry. The material was assumed to be linear elastic with modulus $E = 70$ GPa and Poisson's ratio of $v = 0.3$. A load of 1 N was applied instantaneously at time zero. In a linear elastic material, the stress state and energy release rate would oscillate forever. To eliminate the oscillations, a damping force was applied to each particle proportional to the amplitude of the particle's velocity but in the
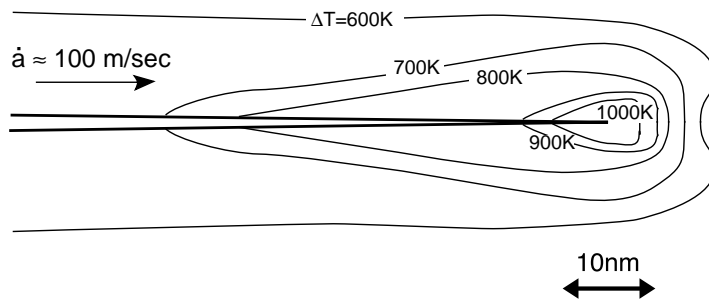

Figure 19 Transient isotherms of temperature rise ΔT caused by a running crack. The crack grows at 100 m s^{-1} in a material following a Mooney–Rivlin constitutive law in which all the fracture energy ($G_c = 100 \text{ J m}^{-2}$) is released as heat. In the figure, the size of the crack tip high plastic zone is ~ 10 nm.
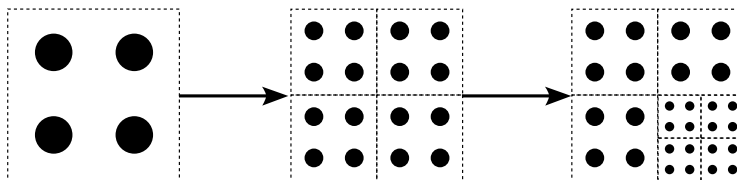

Figure 20 The left side shows the initial material points in a single cell. If $R_{\text{cell}}^{(c)} > R_{\text{crit}}$, any cell can refine by splitting all material points in that element into four new material points. The refinement can continue for more levels as required by the problem being analyzed.

opposite direction. At long times, these damped MPM calculations should converge to static loading of an end-loaded DCB specimen for which all velocities approach zero, the damping term ceases to contribute, and thus the response is linear elastic.

MPM calculations were compared both with and without adaptive meshes. The grid in Figure 21 shows the grid at the start of the calculation that uses uniform, square elements. Figure 22 shows the crack tip region of the mesh at later stages in the calculation. The top half of the figure plots $R_{\text{cell}}^{(c)}$ for the cells in the

plane of the crack. The bottom half of the figure shows the adaptive mesh reflected across the midplane for clarity. In this calculation, the cells around the crack tip refine. After one level of refinement, however, all $R_{\text{cell}}^{(c)}$ drop below R_{crit} and adaptation stops.

Dynamic energy release rate is calculated using crack closure based on the MPM results. Figure 23 plots the MPM results for $G(t)$ calculated with a regular grid or an adaptive grid and calculated with a lumped mass matrix or a full mass matrix. At long times, the numerical results should approach the exact
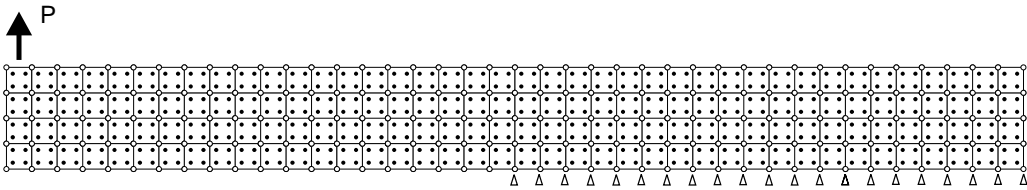
Figure 21 The initial unrefined, background grid for the MPM calculations of a DCB. The mesh is for only half the specimen; the other half is found by symmetry. The specimen is end-loaded with load P. The crack tip is at the first constrained node in the middle of the specimen.

Figure 22 An adaptive mesh calculation when $R_{\text{crit}} = 0.03$. The top half of the plot gives the average value of R_{cell}^{c} in the elements along the crack. The bottom half shows the adapted mesh reflected about the mid-plane for clarity.

static result. Refining the mesh near the crack tip appears to be more efficient to get accurate results.

8.12.4.5.5 *Lattice material point*

SX0550 A LMP has double identities—a lattice from an atomistic perspective and a material point from a continuum perspective. Providing a smooth transition between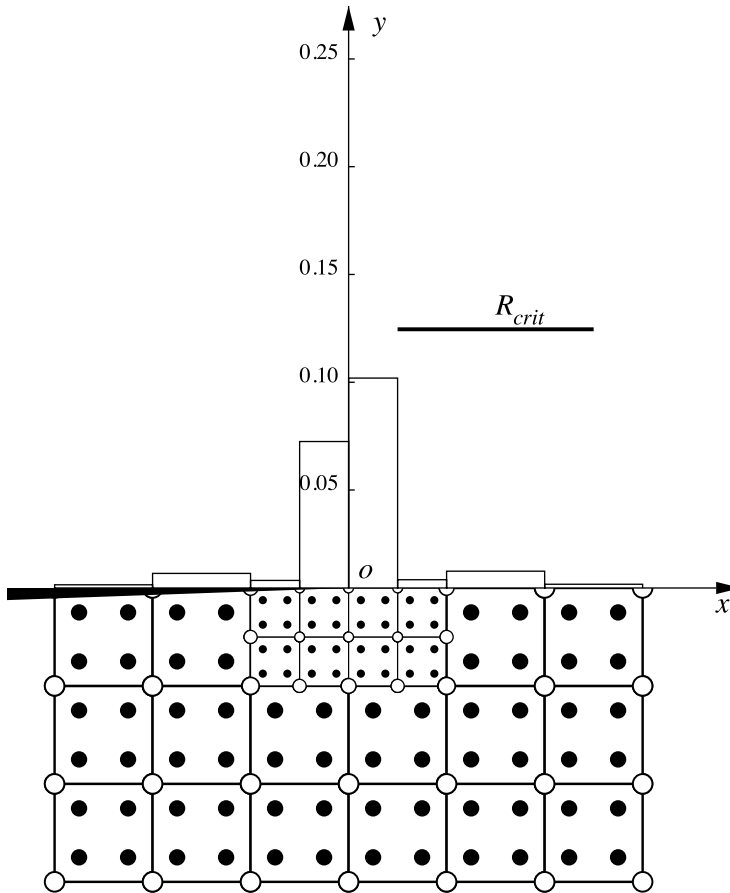 these two representations is the spirit of LMPM. From an atomistic point of view, a LMP represents a lattice, a set of atoms. Each LMP has corner points to define the occupied space. Figure 24 shows a 2D LMP and its four corner points before and after deformation. The corner points update the position according to the interpolated velocity field from the MPM grid. The movement of the lattice atoms is not explicitly calculated.

When continuum to atomistic transition is SX0551 required, the motion of each atom contained in a LMP should be explicitly tracked. The lattice atoms will be released from LMP with velocities interpolated from the background MPM grid plus thermal disturbance related to LMP temperature.

When atomistic to continuum transition is SX0555 required, the positions and velocities of the LMP can be extracted as the average value of the associated atoms. From a continuum point of view, an LMP represents a material point, which can map information on to the grid, and interpolate updated information back from the grid. For MD computation, information about atom position and velocity is sufficient. However, for thermomechanical continuum computation, extra information about stresses and temperature is required. The LMP continuum stresses are the average of atomic stresses,
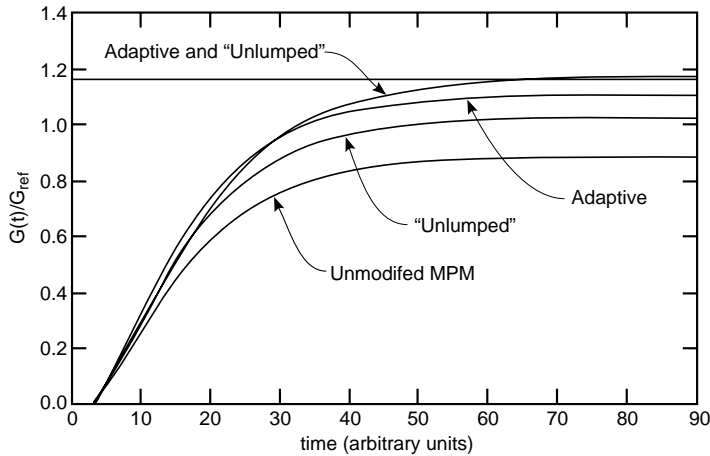
Figure 23 Dynamic energy release rate calculated by four different methods. The "Unmodified MPM" and "Unlumped" results used the regular mesh shown in Figure 21. The two "Adaptive" results started with that mesh but included refinement in the crack-tip region during the calculations. The horizontal line is the "exact "result from the beam-on-elastic-foundation model. All results are normalized to a reference energy release rate, G_{ref}, defined as the simple beam theory result for a DCB.
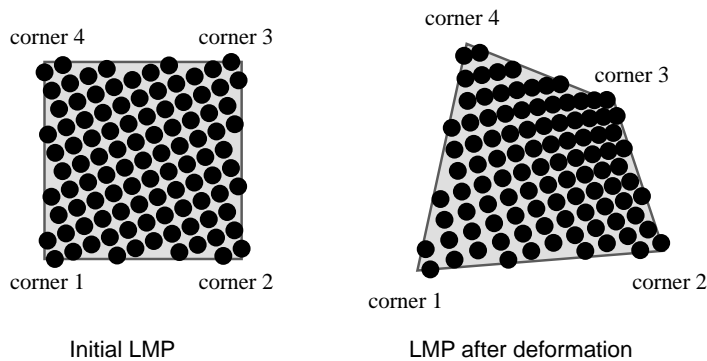
Figure 24 LMP corner points and atoms aggregate. In a 2D description, a LMP has 4 corner points and is initially a square that contains the lattice atoms. The corner points move in the deformation field. Movement of the included lattice atoms is interpolated from the LMP corners.

which can be evaluated through statistical average of the force on each atom from the local neighboring atoms. The stress tensor with respect to an atom α is evaluated by

$$\sigma_{ij}^{(\alpha)} = \frac{1}{2\Omega^{(\alpha)}} \sum_{\beta \neq \alpha}^{\text{neighbors}} V'(r^{(\alpha,\beta)}) \frac{r_i^{(\alpha,\beta)} r_j^{(\alpha,\beta)}}{r^{(\alpha,\beta)}} \quad (81)$$

where $\Omega^{(\alpha)}$ is the atomic volume of atom α, V is the interatomic potential, $r^{(\alpha,\beta)}$ is the distance between atom α, and atom β, $r_i^{(\alpha,\beta)}$ is the ith component of the vector pointing from atom β to atom α. The LMP temperature can be measured from the associated atomic velocity distribution.

SX0560   Continuum material point can be refined to the nanoscale. However, there is a limit for the refinement. From the requirement of atomic stress analysis, the minimum size of a material point should not be smaller than the neighbor size as needed for the above atomic stress calculations. There is also a lower limit on the number of atoms associated in temperature analysis.

8.12.4.5.6   Connectivity between the atomistic and continuum regions

SX0565   LMPM uses a uniform background grid that hosts both continuum and atomistic cells. The simulation region is divided into two regions—an atomistic region and a continuum region; grid nodes connect two regions. In the continuum computations, the grid serves as an interpolation space for solving the continuum equations. In an atomistic computation, the grid helps to define the particle neighbors. The separation of continuum from atomistic regions is dynamic and is adapted during the simulation.

Nodes at the interface between the conti-   SX0570 nuum and atomistic regions, such as node m in Figure 25, collect stress and temperature information from LMP in both continuum and atomic side. The stress and temperature calculations are described in the last section for LMP in atomic sides. After forming the nodal force and temperature gradient, the motion and temperature equations can be solved. On the continuum side, the continuum LMP will interpolate the value from grid nodes and update. On the atomic side, the MD simulation needs the information of neighboring atomic positions to compute the energy potential, thus the force on each atom. The position of neighbor atoms in the continuum side can be interpolated from the LMP corners.

8.12.4.5.7   Application

Novel superhard nanocomposites with Vick-   SX0575 ers hardness of more than 40 GPa have been developed in recent years (Veprek, 1999; Veprek and Argon, 2002). Tan and Yang (1998) identified three toughening mechanisms in Al_2O_3/nano-SiC composite ceramics: (i) switching from intergranular to transgranular cracking due to nanoparticles along the grain boundaries, (ii) fracture surface roughening, or a zigzag crack path promoted by the internal stresses caused by nanoparticles within the grains, and (iii) shielding by clinched rough surfaces near the crack tip. Using LMPM, Tan (2001) simulated an intergranular crack that is propagating to an intergranular nanoparticle SiC under mode I extensional load. As shown in Figure 26, the matrix grain is Al_2O_3. The simulation shows where the crack goes under different dynamic loading magnitudes and rates, interfacial bonding properties, and background residual stresses. The atomistic lattice
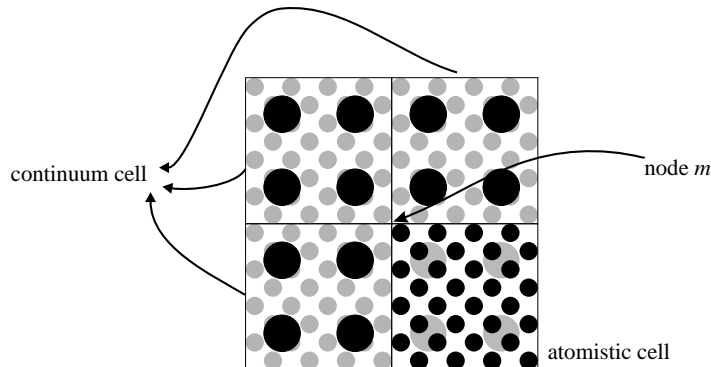

Figure 25   Connection between the continuum and the atomistic regions. In the continuum region, material points (black particles) are tracked explicitly using continuum MPM. The corresponding lattice atoms (gray particles) are used only for linking with the atomistic region as neighboring atoms. In the atomistic region, lattice atoms (black particles) are tracked explicitly using MD.
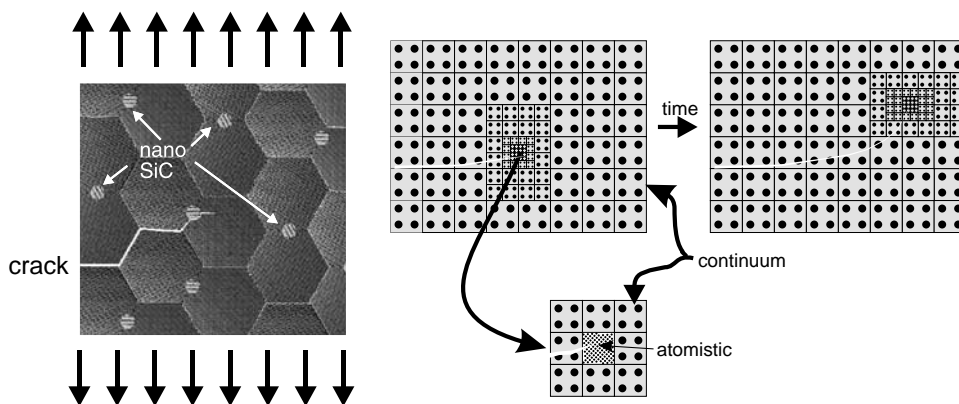
Figure 26 Combined continuum/atomistic simulations of crack-tip process zones when a transgranular crack is approaching an intergranular nanoparticle. There is mode I tensile load applied in the far field and nanoscale residual stresses around the nanoparticle.

follows the crack tip as it moves along the grain boundary, matrix/nanoparticle interface, or enters the matrix grain. The matrix grain far from the crack tip is computed using continuum MPM. The simulation shows that strong cohesion between the nanoparticles and the matrix steers the crack into the matrix grain.

SX0580   Ayton *et al.* (2001) developed a computational methodology including the continuum level simulation using MPM as well as the microscopic method of nonequilibrium MD. They examined the behavior of a membrane bilayer/solvent system using this micro-to-macro dynamical feedback simulation technique. With this method, two simulations at different time and length scales are interfaced into a unified simulation methodology. The interface is accomplished via an information transfer where selected material properties (transport coefficients) and state parameters (density) are calculated in one spatial/temporal regime and then used as initial input in another. What results is a closed feedback loop.

8.12.4.6 Compound Wavelet Matrix Method

SX0585   Frantziskonis and Deymier (2000) designed compound wavelet matrix (CWM) method to bridge multiscale models over different ranges of spatial and time scales. Based on wavelets that can establish a bridge between simulation techniques, CWM captures the physics at significantly different scales as long as there exists a region of overlap in the domain of scales.

SX0590   CWM was introduced to study grain growth. Normal grain growth achieves a quasistationary distribution of grain sizes after a transient period. Understanding grain growth necessi-

tates an accurate description of the spatial and temporal evolution of polycrystals during this transient and, more importantly, the quasistationary stage of the process.

Two computational methodologies exist to   SX0595 describe the grain growth. On the finer scale is the MD simulation of the Lennard–Jones (L–J) system. On the coarser scale is the MC simulation of the Q-states Potts model. Two methods are applied to a region of material simultaneously. Matrices of the wavelet coefficient are produced from energy maps representing the spatial distribution of the local excess energy in the microstructures obtained with both methodologies. The full description of the material then is obtained by merging the matrices of the wavelet coefficients representing the material at different scales through the CWM method. The CWM then characterizes the materials over a range of scales that is the union of the scales treated by the two methodologies. This method possesses several advantages. First, it does not assume *a priori* that a collection of small microscale systems is equivalent to a microscale-based model of a large system. Second, the simulation time of the coarsest methodology is not controlled by the methodology with the slowest dynamics.

To illustrate the CWM method applied to   SX0600 2D grain growth, an MD simulation of a 2D L–J system and an MC simulation of a Q-states Potts model that can overlap over a range of spatial and time scales was presented. These simulations were bridged by the overlap in scale of the "mesoscopic" Q-states Potts model with the atomistic L–J model.

Figure 27 shows a schematic diagram of the   SX0605 construction of the CWM on a 2D grain-growth problem described as L–J system on a finer scale and Potts system on a coarser scale. After having established a correspondence
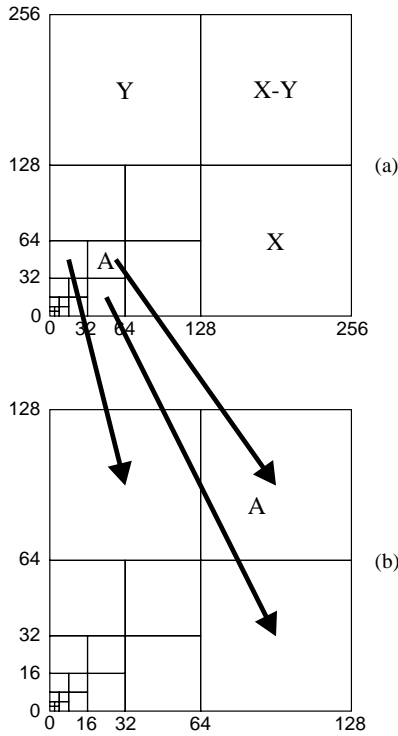
Figure 27 Schematic diagram of the construction of the CWM: (a) from the L–J system of 1×1 units of length discretized into 256×256 points and (b) from the Potts system of 2×2 units of length discretized into 128×128 points. The arrows indicate the substitution (transfer of matrix statistics) of matrices in forming the compound matrix. Only three such substitutions are shown for illustration (after Frantziskonis and Deymier, 2000).

between the L–J model and the Q-states Potts model of microstructures and their evolution, wavelet transforms can be used to analyze microstructures scale-wise as well as to bridge the L–J system to the Potts model. As an example, consider an L–J system of 1×1 units of length discretized into 256×256 points. Next consider a larger Potts system with a physical size of 2×2 units of length discretized into 128×128 points. Figure 27 illustrates the construction of the compound matrix. Considered in Figure 27(a) are the wavelet coefficients of the L–J system and in Figure 27(b) are those of the Potts system. Note that the discretization and the units of length can vary, and this is only an example illustrating the ideas. The problem addressed herein is that the Potts system cannot represent the details "seen" by the L–J system. Submatrix A shown SX0610 in Figure 27(b) represents the details appearing when 2×2 units of length are discretized into 64×64 points; yet this is equivalent to 1×1 units of length discretized into 32×32 points. The same type of discretization (1×1 units,

32×32 points) in the L–J system is represented by submatrix A in Figure 27(a). Thus, by making the substitutions as indicated by the arrows, the compound matrix has now statistical information at those scales not "seen" by the Potts model, yet seen by the L–J models. Of course, all the corresponding matrices (those with corresponding scale and discretization) are substituted, yet only three such substitutions are shown in Figure 27. The compound matrix is a representation of the microstructure over the range of scales. Now it represents the union of the scales of the L–J and Potts systems.

Consider simple and classical "versions" of SX0615 two simulation methods (MD and MC) and concentrate on their bridging and their overlapping over a region of scales. In CWM method, a large L–J system is statistically equivalent to the combined models of Potts and small L–J. The method of classical MD consists of solving simultaneously the equations of motions of an assembly of particles interacting with each other through some interatomic potential. The MD method is atomistic and allows investigation of grain growth from the atomic scale up, yet it is limited (by computer power) to small numbers of particles (nowadays in the hundreds of millions) and short periods of time. The microstructure is characterized by calculating the excess atomic potential energy of each individual atom (relative to the potential energy of an atom in a perfect lattice at the same temperature). The excess atomic energy is then normalized by the total excess energy of the microstructure at $t = 0$. The spatial distribution of the normalized excess atomic energy is then mapped onto a 512×512 square matrix to obtain what will be referred to as an energy map. Note that the L–J system includes grain boundary anisotropy. The grain boundary energy varies with the degree of misorientation between adjacent grains. A microstructure may, therefore, contain low-energy low-angle grain boundaries and high-energy high-angle grain boundaries. Moreover, the anisotropy in the grain boundary energy also results in fixed misorientation from the inclination of the grain boundary plane.

In an MC simulation of grain growth with a SX0620 Potts model, both spatial and "MC time" scales are coarser than those in MD. The Potts model maps the microstructure onto a discrete lattice that is coarser than the atomic scale, and the "spin" state $S = 1, ..., Q$ of each lattice site represents the orientation of the grain in which it is embedded. A grain boundary exists between two adjacent lattice sites with different orientations. Now employ a Potts model with a

square lattice containing 128×128 sites and $Q = 10$ (see following discussion) with only the nearest-neighbor interactions. This model is designed to represent a piece of material with dimensions similar to those of the MD system. A square lattice is chosen to mimic anisotropic grain growth.

SX0625 An MC algorithm is used to evolve this model. Initial microstructures are produced from totally random configurations. A total of four such initial configurations corresponding to microstructures optically similar to the initial configuration of the L–J system are thus obtained (the similarity between the initial Potts microstructures and the initial L–J system was further confirmed by their wavelet transformation showing similar statistics at the equivalent scales). Subsequently, long MC simulations were run to anneal the initial microstructures, until the total energy averaged over the four systems decreased to nearly 63% of the average energy of the initial configurations. Matrices of size 128×128 containing the value of energy at every lattice site characterize the final MC microstructures. Note that the energy in the Potts model represents an excess energy relative to a perfectly ordered system (perfect crystal). Normalization of the energy at each lattice site by the total excess energy of the initial microstructure allows a direct comparison with the energy maps produced from the MD simulations.

SX0630 In order to bridge the two simulation techniques, correspondence should be established between the MD and MC times and energies. Several approaches have been proposed in the literature; e.g., MC time can be related linearly to real time (Ling and Anderson, 1998). The conversion from the MC time to real time has an implicit activation energy factor that corresponds to a jump. On the other hand, in the Potts model a grain boundary exists between two adjacent lattice sites with different orientations. Therefore, the time for reorientation of a lattice site may be related to the time for migration of a segment of a grain boundary. On this premise, a time conversion scheme, based on grain boundary migration, may be applicable (Gao and Thompson, 1996).

SX0635 Wavelet method is suitable for multiscale simulation. The different scales can be either the wave numbers corresponding to spatial variables or the frequencies corresponding to temporal variables, and each scale response can be examined separately. Liu and Chen (1995) and Liu *et al.* (1996, 1997) introduced wavelet into the meshless unstructured adaptive refinements. A space-scale and time-frequency localization process is achieved by dilating the flexible multiple scale window function.

8.12.4.7 Numerical Simulations of Hydrogen–Plasticity Interaction

Hydrogen induced plasticity is increasingly SX0640 invoked in many SCC cases. Sydow and Wahnström (1996) carried out MD simulations for hydrogen diffusion in niobium. They found that hydrogen reduces the velocities of dislocations and that the hydrogen distribution in the glide-plane is essentially unaffected by that motion. Zhou *et al.* (1998) studied the effects of hydrogen on the dislocation emission from a crack tip. The simulated results showed that hydrogen reduced the cohesive strength for aluminum single crystal. The simulation also shows that hydrogen atoms can gather and turn into small bubbles, resulting in enhancement of the equilibrium vacancy concentration. Delafosse *et al.* (1999) examined by simulation the effect of hydrogen on the density of a dislocation pile-up. The particular situation at the tip of a loaded crack is examined via the introduction of image forces on diffusing interstitial hydrogen. Baranov *et al.* (2000) simulated crack propagation in hydrogen-containing α-iron using MD method and found hydrogen formed Cottrell clouds around dislocations, thus suppressing their movement and generation. In addition, an increase in the hydrogen concentration in iron near the crack mouth makes the material more prone to $\alpha \rightarrow \gamma$ phase transition. As a result, crack propagation is observed, i.e., the material embrittles.

It is important to show how hydrogen– SX0645 plasticity interactions evolve during SCC of engineering materials. Delafosse and Magnin (2001) investigated the interaction between hydrogen and mobile dislocations by means of a set of equations in which the diffusion and stress gradients are coupled. The problem of crack hydrogen–dislocation interactions in the case of SCC crack tip is investigated within this framework.

The first order elastic interactions between SX0650 diffusing hydrogen and mobile dislocations stem from the dilatation strains induced by the presence of hydrogen in interstitial octahedral sites in the austenitic matrix. This is characterized by the partial molar volume, V^*, and the unconstrained volume dilatation of the host metal due to the introduction of 1 mol of hydrogen. If H is the expansion tensor associated with one hydrogen atom, the strain tensor due to a hydrogen concentration C is purely hydrostatic:

$$\varepsilon_{ij} = H_{ij}(C - C_0)N_{av} = \tfrac{1}{2}(C - C_0)V^*\delta_{ij} \quad (82)$$

where C_0 is the concentration in the reference state, N_{av} is Avogadro's number, and δ is the

Kroneker delta. In the presence of a stress field, the chemical potential of a hydrogen atom in solid solution is given by Sofronis (1995),

$$\mu = \mu_0 + kT \ln\left(\frac{C}{C_0}\right) - H_{ij}\sigma_{ij}$$

$$= \mu_0 + kT \ln\left(\frac{C}{C_0}\right) - \frac{V^*}{N_{av}}\frac{\sigma_{kk}}{3} \qquad (83)$$

From this, the first and second Fick's laws are derived and are seen to include stress-induced terms:

$$\mathbf{J} = -\frac{D_H C}{kT}\nabla\mu = -D_H\nabla C + \frac{D_H V^*}{RT}C\nabla\frac{\sigma_{kk}}{3} \quad (84)$$

and

$$\frac{\partial C}{\partial t} = -\nabla\cdot\mathbf{J}$$

$$= D_H\nabla^2 C - \frac{D_H V^*}{RT}\left(C\nabla^2\frac{\sigma_{kk}}{3} + \nabla C\cdot\nabla\frac{\sigma_{kk}}{3}\right) (85)$$

where D_H is the diffusion coefficient of hydrogen at temperature T and R is the ideal gas constant. The diffusion equation is solved numerically within a finite difference scheme on a square grid with a typical node spacing of 2 nm.

SX0655   The coupled elasticity-diffusion equations are applied to elementary configurations consisting of one isolated edge dislocation and two coplanar edge dislocations. Because of its positive partial molar volume, hydrogen diffuses from the compression zones towards the zones under hydrostatic tension. Figure 28(a)

presents the concentration profile. It can be seen that the iso-concentration lines precisely map the contours of the hydrostatic stress around the dislocation. When computing the sum of the hydrostatic stresses stemming from the local concentration in each box, one can see that the antisymmetrical hydrogen distribution with respect to the slip plane yields a net shear stress with the same singularity but with a sign opposite to that of the resolved shear stress of the mere dislocation (Figure 28(b)). In other words, the equilibrium hydrogen distribution screens the resolved shear stress of an edge dislocation.

8.12.4.8 Continuum Fluid and Atomistic Surface Hybrid Simulation

The challenge in continuum fluid and   SX0660
atomistic surface hybrid simulation is that the particles follow random trajectories and mass flow across the continuum–particle interface may occur. Several multiscale coupling schemes designed specifically to explore hydrodynamic problems were presented. O'Connell and Thompson (1995) studied the Couette flow problem using an overlap region mediating between a particle ensemble and a continuum described by the incompressible Navier–Stokes equation. This approach is limited to scenarios in which there is no mass and energy exchange between the discrete and the continuous phases. Moreover, in their model momentum is conserved only in the special case in which the continuum equations exactly describe the
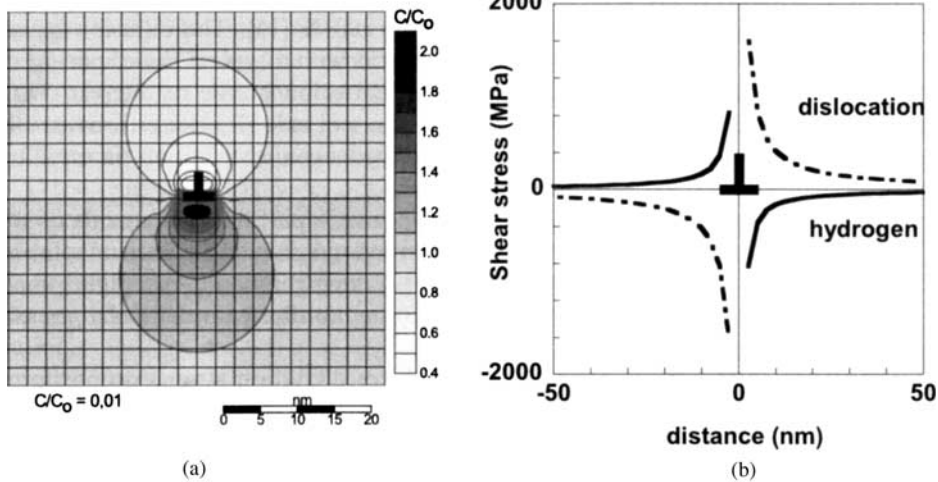
Figure 28 (a) Equilibrium hydrogen distribution around a single edge dislocation at $T = 300$ K. The hydrogen migrates from the "upper" side of the dislocation (compression) to the "lower" side of the glide plane (tensile zone). (b) The sum of the dilatation strains due to the hydrogen anti-symmetric distribution gives a shear stress profile along the glide plane which is similar to that of the dislocation, but with opposite sign. The net effect is a relaxation of the resolved shear stress of the dislocation (after Delafosse and Magnin, 2001).

particle system. Li *et al.* (1998) studied the general problem of obtaining boundary conditions from a particle ensemble. Hadjiconstantinou (1999a, 1999b) used the flow field observed in conventional MD simulations to provide the boundary conditions for separate FE computations. Thus microscopic and macroscopic length scales were coupled elegantly, at the price of limiting the approach to the study of steady-state solutions. Garcia *et al.* (1999) coupled multigrid continuum equations to a direct simulation MC particle simulator. This sophisticated approach includes the exchange of mass, momentum and energy but is limited to dilute systems.

SX0665   Differential equations for continuum fields describe many macroscopic phenomena. Hydrodynamics, e.g., is described by the Navier–Stokes equations, and their solutions depend on boundary conditions. However, boundary conditions are set by the interactions at the atomistic or molecular scale. Flekkoy *et al.* (2000) introduced a "hybrid model" that permits a continuum description in one region to be coupled to an atomistic description in another region. The coupling is symmetric in the sense that the fluxes of the conserved quantities are continuous across the particle–field interface.

SX0670   Lam and Vlachos (2001) introduced multi-scale integration hybrid (MIH) algorithms to model catalytic reactors, epitaxial growth, chemical vapor deposition, and flow through tubes. The basic idea of MIH algorithms is to decompose the domain into two subdomains, one for the macroscopic scale (fluid phase) and one for the microscopic scale (top layers of the film). The partial differential equations characterizing the fluid phase are then discretized and solved through a conventional method, such as finite difference scheme and Newton's algorithm for steady state or the method of lines for time-dependent situations. The surface is modeled with a master equation (a stochastic partial differential equation) that is solved using a continuous time MC algorithm. The coupling of the two subdomains is done at the fluid-film interface through a homogenization of the boundary conditions, i.e., incorporation of mesoscopically average rates computed from molecular model into the boundary conditions of the fluid phase model.

8.12.5   PARALLEL ADAPTIVE MESH REFINEMENT

SX0675   The goal of combined atomistic and continuum simulation is to follow the atomic aggregates adaptively with regions where na-

noscale size effects are important, and to simulate all the remaining regions using continuum method with adaptive mesh refinement towards the atomic core. As of early 2000s, all the simulations are in research stage. In order for combined atomistic and continuum simulation to be practical and to get the industry strength, techniques on parallel adaptive mesh refinement (AMR) are crucial.

SX0680   The parallelization of an AMR algorithm offers challenges. Implementations of AMR algorithms are typically quite complex. The individual grid-patches of an AMR algorithm are not uniform, and cover a broad span of sizes and shapes. High parallel efficiency is achieved by maintaining an equal distribution of work among processors. Otherwise processors will be forced to wait in idleness while an overburdened processor completes its work. Maintaining an equal distribution of work among processors is an issue when the work quanta are not uniform, as is true in AMR with grid objects of greatly differing sizes. Since the results of the competition for resources cannot be predicted at compile time, it is necessary to adjust the work distribution as the parallel program runs.

SX0685   In order for the combined atomistic and continuum simulation to take advantage of the power of parallel computing the code should be built on a parallel AMR infrastructure library. The goal of a parallel AMR library is to facilitate the development of structured AMR applications involving coupled physics models and sophisticated numerical solution methods. The library should provide flexible and extensible tools for structured AMR applications. The library should contain a suite of well-designed, and efficiently implemented, modules that perform operations in a typical parallel AMR process. As shown in Figure 29 the combined atomistic and continuum simulation can interact with AMR infrastructure through (a) hierarchy and data structure management as detailed in Figure 30, (b) algorithm framework, and (c) numerical routines.

SX0690   There are two kinds of AMR, structured and unstructured. Structured methods employ a hierarchy of nested mesh levels in which each level consists of many simple, rectangular grids. Each rectangular grid in the hierarchy represents a structured block of many thousands of unknowns. Unstructured adaptive methods store the solution using graph or tree representations; these methods are called "unstructured" because connectivity information must be stored for each unknown. Because of these dissimilar data representation strategies, structured adaptive methods require
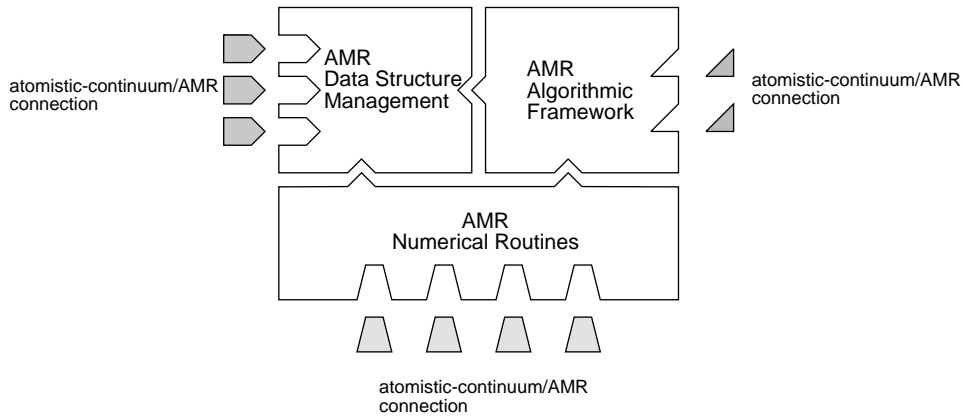
Figure 29 Parallel AMR software provide framework on connection with combined atomistic and continuum simulation.
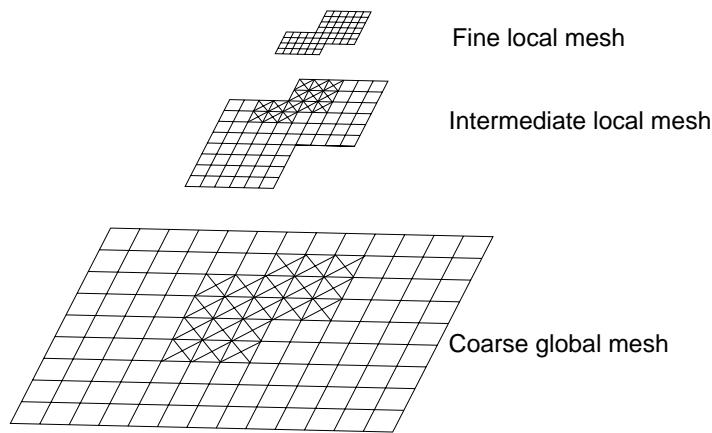

Figure 30 SAMRAI provides management on adaptive mesh refinement. The crossed cells need further refinement.

different software support and implementation approaches than unstructured methods.

8.12.5.1   Structured AMR

Structured local mesh refinement possesses numerous advantages over less structured mesh approaches (Garaizar *et al.*, 1998). These advantages are due primarily to the description of the mesh in terms of a hierarchy of global index spaces and patches suitable for the storage of most mesh data in logically rectangular arrays. The patch-based structured AMR approach provides a paradigm in which applications can be composed of a relatively small set of computationally rich tasks, defined in terms of operations on mesh patches, organized in a highly structured fashion.

A significant amount of research and development has been done to create robust software tools for the fundamental tasks associated with mesh management on parallel computers. As of early 2000s, there are several parallel structured-AMR libraries available. The SAMRAI (Structured Adaptive Mesh Refinement Application Infrastructure) library is an object-oriented C++ software framework. SAMRAI is supported by the Lawrence Livermore National Laboratory and the US Department of Energy's Accelerated Strategic Computing Initiative program. The PARAMESH (PAR-Allel adaptive MESH refinement), supported by NASA's High Performance Computing and Communications program, provides a package of Fortran 90 routines.

8.12.5.2   Parallel LMPM Simulation Based on SAMRAI

In the following we discuss how to connect
LMPM with SAMRAI parallel infrastructure. In SAMRAI, the "Hierarchal" package supports abstract index spaces and box calculus on which most operations on a structured AMR patch hierarchy depends. Structural classes such as patch, patch level, and patch hierarchy,

and base classes for managing variables and data living on the hierachy also reside here.

SX0710   LMPM provides for the skeletal SAMRAI grid structure with detailed material points as shown in Figure 30. In LMPM, a continuum material is discretized into a collection of material points in a manner similar to representing an image with pixels. Each material point is assigned a mass consistent with the material density and all the variables describing the problem (e.g., position, velocity, strain, stresses, temperature, etc.). LMPM then uses a background calculation grid to solve the equations of motion for the particles at each time step of the analysis.

SX0711   LMPM uses SAMRAI's hierarchy management to handle splitting and merging of LMPM cells and particles. In 3D, one cell can be split into eight child cells, forming an oct-tree structure. Figure 20 shows the splitting of cells and material points in LMPM calculation (2D case). In the refining and coarsening process, the state variables of the material points are interpolated to the new points, such that the interpolated values of variables onto the grid are the same before and after the refining/coarsening process. In the finest level, all the atoms are uniformly distributed in the paralleled processors.

SX0715   In SAMRAI, cells on each hierarchical level are clustered to form logically rectangular patches. SAMRAI's "PatchData" package provides support for various concrete patch data types that reside on a structured AMR patch hierarchy. LMPM uses SAMRAI's node-centered PatchData to implement node information such as velocity, acceleration, mass, temperature and temperature gradient. LMPM uses SAMRAI's particle PatchData to implement atomic information, as well as material points information, such as particle position, velocity, mass, stresses, and temperature.

SX0720   In SAMRAI, the "Algorithm" package houses classes that are useful for constructing solution algorithms for certain classes of partial differential equations on a structured AMR patch hierarchy. Basic MPM algorithm includes three steps in each time step integration cycling. They are: (i) map particle information to grid, (ii) solve motion equations on grid, and (iii) interpolate grid information to particles. This MPM basic algorithm was implemented into the SAMRAI (CSAFE, 1999).

SX0725   The kernel motion and thermal equations in LMPM are Equations (67) and (77), respectively, with atomistic modifications discussed in Section 8.12.4.5.1. Use of "unlumped" mass-matrix can give higher accuracy. However, this requires solving a large system of equations. The SAMRAI "Solver" package provides support for applying linear, nonlinear, and ODE solvers on a structured AMR patch hierarchy. The LMPM's unlumped mass-matrix motion and thermal equations can be solved with these solvers.

8.12.5.3 Unstructured AMR

SX0730   There are several parallel unstructured-AMR libraries available. The PYRAMID, developed at California Institute of Technology under support from NASA, is a software library for performing parallel AMR on unstructured meshes (Norton *et al.*, 2001). The main structure is the computational mesh that represents a complex geometry with many components. Object-oriented methods, using $C++$, have been applied to manage the complexity for this problem. Another software, SUMAA3D (Scalable Unstructured Mesh Algorithms and Applications), represents collaborative efforts from Argonne National Laboratory, Penn State University, Virginia Tech., and The University of British Columbia.

8.12.6 CONCLUDING REMARKS

SX0735   Major multiscale numerical methods in simulations for fracture and corrosion are reviewed. Both lattice Green's function and QC methods are static methods. These methods are effective in seeking long-term balanced configurations, and time scale is not a difficult issue in these approaches. However, as shown in Section 8.12.2, dynamic effects are important at nanoscale. Coupled FE/MD and LMPM provide dynamic solution. In FE/MD coupling, one-to-one node/atom connection provides extra constraint and blocks the movement of atomic defects into continuum region. Overlapping approach gives a more flexible solution. MPM/MD coupling has advantages over FE/MD coupling in parallel simulation, adaptivity, large deformation, uniform continuum, and atomic descriptions. However, because both FE/MD and LMPM are dynamic methods, they suffer from atomic timescale simulations. WCM and adaptive LMPM provide coupling not only in space but also in time. The material point/atoms linkage in LMPM has some similarity with CGMD, where a material point can be viewed as a CG atom group.

SX0740   Most of the current parallel AMR libraries are still projects in the developing and optimizing stage. Depending on the methodology chosen, all combined atomistic and continuum simulations will finally be built on a parallel

AMR infrastructure in order to use the super-computing resources. In the future, the parallel version of LMPM can be developed based on SAMRAI or a similar structured parallel AMR library, parallel version of QC and coupled FE/MD can be developed based on PYRAMID or a similar parallel unstructured-AMR library.

8.12.7   REFERENCES

F. F. Abraham, 2001, The atomic dynamics of fracture. *J. Mech. Phys. Solids*, **49**, 2095–2111.

F. F. Abraham, N. Bernstein, J. Q. Broughton and D. Hess, 2000, Dynamic fracture of silicon: Concurrent simulation of quantum electrons, classical atoms, and the continuum solid. *MRS Bull.*, **25**, 27–32.

F. F. Abraham, D. Brodbeck, R. A. Rafey and W. E. Rudge, 1994, Instability dynamics of fracture: a computer-simulation investigation. *Phys. Rev. Lett.*, **73**, 272–275.

F. F. Abraham, D. Brodbeck, W. E. Rudge and X.-P. Xu, 1997a, A molecular dynamics investigation of rapid fracture mechanics. *J. Mech. Phys. Solids*, **45**, 1595–1619.

F. F. Abraham, J. Q. Broughton, N. Bernstein and E. Kaxiras, 1998, Spanning the length scales in dynamic simulation. *Comp. Phys.*, **12**, 538–546.

F. F. Abraham and H. Gao, 2000, How fast can cracks propagate? *Phys. Rev. Lett.*, **84**, 3113–3116.

F. F. Abraham, D. Schneider, B. Land, D. Lifka, J. Skovira, J. Gerner and M. Rosenkrantz, 1997b, Instability dynamics in three-dimensional fracture: an atomistic simulation. *J. Mech. Phys. Solids*, **45**, 1461–1471.

D. J. Andrews, 1976, Rupture velocity of plane strain shear cracks (earthquake model). *J. Geophys. Res.*, **81**, 5679–5687.

C. E. Aumann, G. L. Skofronick and J. A. Martin, 1995, Oxidation behavior of aluminum nanopowders. *J. Vac. Sci. Technol. B*, **13**, 1178–1183.

G. Ayton, S. G. Bardenhagen, P. McMurtry, D. Sulsky and G. A. Voth, 2001, Interfacing continuum and molecular dynamics: an application to lipid bilayers. *J. Chem. Phys.*, **114**, 6913–6924.

M. A. Baranov, A. Y. Drozdov, V. G. Chudinov and V. Y. Bayankin, 2000, Atomic mechanisms of microcrack propagation in pure and hydrogen-containing FCC and BCC metals. *Tech. Phys.*, **45**, 427–431 (in Russian).

S. G. Bardenhagen, J. U. Brackbill and D. Sulsky, 2000, The material-point method for granular materials. *Comp. Methods Appl. Mech. Eng.*, **187**, 529–541.

S. G. Bardenhagen, J. E. Guilkey, K. M. Roessig, J. U. Brackbill, W. M. Witzel and J. C. Foster, 2001, An improved contact algorithm for the material point method and application to stress propagation in granular material. *Comp. Model. Eng. Sci.*, **2**, 509–522.

G. E. Beltz and D. M. Lipkin, 2000, A dislocation model for the directional anisotropy of grain-boundary fracture. *MRS Bull.*, **25**, 21–26.

S. W. J. den Brok and J. Morel, 2001, The effect of elastic strain on the microstructure of free surfaces of stressed minerals in contact with an aqueous solution. *Geophys. Res. Lett.*, **28**, 603–606.

R. Burridge, 1973, Admissible speeds for plane-strain self-similar shear cracks with friction but lacking cohesion. *Geophys. J. Roy. Astron. Soc.*, **35**, 439–455.

R. Burridge, G. Conn and L. B. Freund, 1979, Stability of a rapid mode II shear crack with finite cohesive traction. *J. Geophys. Res.*, **84**, 2210–2222.

T. Campbell, R. K. Kalia, A. Nakano, P. Vashishta, S. Ogata and S. Rodgers, 1999, Dynamics of oxidation of aluminum nanoclusters using variable charge molecular-dynamics simulations on parallel computers. *Phys. Rev. Lett.*, **82**, 4866–4869.

E. S. C. Ching, J. S. Langer and H. Nakanishi, 1995, Dynamic stability of one-dimensional models of fracture. *Phys. Rev. E*, **52**, 4414–4420.

CSAFE (Center for the Simulation of Accidental Fires & Explosions) 1999, Annual report, University of Utah to the Department of Energy, Lawrence Livermore National Laboratory.

CSAFE, 2000, Annual report, University of Utah to the Department of Energy, Lawrence Livermore National Laboratory.

CSAFE, 2001, Annual report, University of Utah to the Department of Energy, Lawrence Livermore National Laboratory.

D. Delafosse, J. P. Chateau and T. Magnin, 1999, Microfracture by pile-up formation at a stress corrosion crack tip: numerical simulations of hydrogen/dislocation interactions. *J. Phys. IV*, **9**, 251–260.

D. Delafosse and T. Magnin, 2001, Hydrogen induced plasticity in stress corrosion cracking of engineering system. *Eng. Fract. Mech.*, **68**, 693–729.

J. Fineberg, S. P. Gross, M. Marder and H. L. Swinney, 1991, Instability in dynamic fracture. *Phys. Rev. Lett.*, **67**, 457–460.

J. Fineberg, S. P. Gross, M. Marder and H. L. Swinney, 1992, Instability in the propagation of fast cracks. *Phys. Rev. B*, **45**, 5146–5154.

D. S. Fisher, K. Dahmen, S. Ramanathan and Y. Ben-Zion, 1997, Statistics of earthquakes in simple models of heterogeneous faults. *Phys. Rev. Lett.*, **78**, 4885–4888.

E. G. Flekkoy, G. Wagner and J. Feder, 2000, Hybrid model for combined particle and continuum dynamics. *Europhys. Lett.*, **52**, 271–276.

G. Frantziskonis and P. A. Deymier, 2000, Wavelet methods for analysing and bridging simulations at complementary scales: the compound wavelet matrix and application to microstructure evolution. *Model. Simul. Mater. Sci. Eng.*, **8**, 649–664.

L. B. Freund, 1990, "Dynamic Fracture Mechanics," Cambridge University Press, New York.

Y. Furuya and H. Noguchi, 1998, A combined method of molecular dynamics with micromechanics improved by moving the molecular dynamics region successively in the simulation of elastic-plastic crack propagation. *Int. J. Fract.*, **94**, 17–31.

Y. Furuya and H. Noguchi, 2001, Combined method of molecular dynamics with micromechanics in simulations of crack propagation. *Mater. Trans. JIM*, **42**, 45–51.

Y. Furuya, H. Noguchi and S. Schmauder, 2001, Molecular dynamics study on low temperature brittleness in tungsten single crystals. *Int. J. Fract.*, **107**, 139–158.

H. Gao, Y. Huang and F. F. Abraham, 2001, Continuum and atomistic studies of intersonic crack propagation. *J. Mech. Phys. Solids*, **49**, 2113–2132.

J. Gao and R. G. Thompson, 1996, Real time-temperature models for Monte Carlo simulations of normal grain growth. *Acta Mater.*, **44**, 4565–4570.

F. X. Garaizar, R. D. Hornung, S. R. Kohn and S. G. Smith, 1998, SAMRAI: A framework for structured AMR. In: "Symposium on Adaptive Methods for Partial Differential Equations," University of Utah, Salt Lake City, UT, June 22–24.

A. L. Garcia, J. B. Bell, W. Y. Crutchfield and B. J. Alder, 1999, Adaptive mesh and algorithm refinement using

direct simulation Monte Carlo. *J. Comp. Phys.*, **154**, 134–155.

L. Greengard and V. Rokhlin, 1987, A fast algorithm for particle simulations. *J. Comp. Phys.*, **73**, 325–348.

J. E. Guilkey and J. A. Weiss, 2002, Implicit time integration with the Material Point Method: Quantitative and algorithmic comparisons with the Finite Element Method. *Int. J. Num. Meth. Eng.*, submitted.

G. Guo, W. Yang, Y. Huang and A. J. Rosakis, 2002, Suddenly decelerating or accelerating intersonic shear cracks. Submitted to *J. Mech. Phys. Solids*.

N. G. Hadjiconstantinou, 1999a, Hybrid atomistic-continuum formulations and the moving contact-line problem. *J. Comp. Phys.*, **154**, 245–265.

N. G. Hadjiconstantinou, 1999b, Combining atomistic and continuum simulations of contact-line motion. *Phys. Rev. E*, **59**, 2475–2478.

H. L. Heinisch, 1995, Simulating the production of free defects in irradiated metals. *Nucl. Instrum. Methods Phys. Res. B*, **102**, 47–50.

H. L. Heinisch and B. N. Singh, 1996, Stochastic annealing simulation of differential defect production in high energy cascades. *J. Nucl. Mater.*, **232**, 206–213.

W. G. Hoover, A. J. De Groot and C. G. Hoover, 1992, Massively parallel computer simulation of plane-strain elastic-plastic flow via non-equilibrium molecular dynamics and Lagrangian continuum mechanics. *Comp. Phys.*, **6**, 155–167.

M. F. Horstemeyer, M. I. Baskes, A. Godfrey and D. A. Hughes, 2002, A large deformation atomistic study examining crystal orientation effects on the stress–strain relationship. *Int. J. Plast.*, **18**, 203–229.

M. F. Horstemeyer, M. I. Baskes and S. J. Plimpton, 2001a, Computational nanoscale plasticity simulations using embedded atom potentials. *Theor. Appl. Fract. Mech.*, **37**, 49–98.

M. F. Horstemeyer, M. I. Baskes and S. J. Plimpton, 2001b, Length scale and time scale effects on the plastic flow of fcc metals. *Acta Mater.*, **49**, 4363–4374.

M. Jaraiz, G. H. Gilmer, J. M. Poate and T. D. de la Rubia, 1996, Atomistic calculations of ion implantation in Si: point defect and transient enhanced diffusion phenomena. *Appl. Phys. Lett.*, **68**, 409–411.

R. K. Kalia, S. de Leeuw, A. Nakano and P. Vashishta, 1993, Molecular dynamice simulations of Coulombic systems on distributed-memory MIMD machines. *Comp. Phys. Commun.*, **74**, 316–326.

R. K. Kalia, A. Nakano, K. Tsuruta and P. Vashishta, 1997, Morphology of pores and interfaces and mechanical behavior of nanocluster-assembled silicon nitride ceramic. *Phys. Rev. Lett.*, **78**, 689–692.

K.-S. Kim and J. A. Hurtado, 2000, Length scale effects in nano- and micro-mechanics of solids. *Key Eng. Mater.*, **183–187**, 1–8.

K.-S. Kim, J. A. Hurtado and H. Tan, 1999, Evolution of surface-roughness spectrum caused by stress in nanometer-scale chemical etching. *Phys. Rev. Lett.*, **83**, 3872–3875.

J. Knap and M. Ortiz, 2001, An analysis of the quasicontinuum method. *J. Mech. Phys. Solids*, **49**, 1899–1923.

S. Kohlhoff, P. Gumbsch and H. F. Fischmeister, 1991, Crack propagation in BCC crystals studied with a combined finite-element and atomistic model. *Phil. Mag. A*, **64**, 851–878.

R. Lam and D. G. Vlachos, 2001, Multiscale model for epitaxial growth of films: growth mode transition. *Phys. Rev. B*, **64**, 035401.

J. S. Langer, 1992, Models of crack-propagation. *Phys. Rev. A*, **46**, 3123–3131.

J. Li, D. Liao and S. Yip, 1998, Coupling continuum to molecular-dynamics simulation: reflecting particle method and the field estimator. *Phys. Rev. E*, **57**, 7259–7267.

J. Liang and Z. Suo, 2001, Stress-assisted reaction at a solid-fluid interface. *Interface Sci.*, **9**, 93–104.

E. Lidorikis, M. E. Bachlechner, R. K. Kalia, A. Nakano, P. Vashishta, and G. Z. Voyiadjis, 2001, Coupling length scales for multiscale atomistics-continuum simulations: atomistically induced stress distributions in Si/Si_3N_4 nanopixels. *Phys. Rev. Lett.*, **87**, 086104/1–4.

S. Ling and M. P. Anderson, 1988, Development and evolution of thin film microstructures: a Monte Carlo approach. *J. Electron. Mater.*, **17**, 459–466.

W. K. Liu and Y. J. Chen, 1995, Wavelet and multiple scale reproducing kernel methods. *Int. J. Num. Methods Fluids*, **21**, 901–931.

W. K. Liu, Y. J. Chen, R. A. Uras and C. T. Chang, 1996, Generalized multiple scale reproducing kernel particle methods. *Comp. Meth. Appl. Mech. Eng.*, **139**, 91–157.

W. K. Liu, S. Jun, D. T. Sihling, Y. J. Chen and W. Hao, 1997, Multiresolution reproducing kernel particle method for computational fluid dynamics. *Int. J. Num. Methods Fluids*, **24**, 1391–1415.

K. Masuda-Jindo, M. Menon and V. Van Hung, 2001, Atomistic study of fracture of nanoscale materials by molecular dynamics and lattice Green's function methods. *J. Phys. IV*, **11**, 11–18.

R. Miller, M. Ortiz, R. Phillips, V. Shenoy and E. B. Tadmor, 1998a, Quasicontinuum models of fracture and plasticity. *Eng. Fract. Mech.*, **61**, 427–444.

R. Miller, E. B. Tadmor, R. Phillips and M. Ortiz, 1998b, Quasicontinuum simulation of fracture at the atomic scale. *Modelling Simul. Mater. Sci. Eng.*, **6**, 607–638.

A. Nakano, 1997, Parallel multilevel preconditioned conjugate-gradient approach to variable-charge molecular dynamics. *Comp. Phys. Commun.*, **104**, 59–69.

A. Nakano, 1999, A rigid-body-based multiple time scale molecular dynamics simulation of nanophase materials. *Int. J. High Perform. Comp. Appl.*, **13**, 154–162.

A. Nakano, M. E. Bachlechner, T. J. Campbell, R. K. Kalia, A. Omeltchenko, K. Tsuruta, P. Vashishta, S. Ogata, I. Ebbsjo and A. Madhukar, 1998a, Atomistic simulation of nanostructured materials. *IEEE Comp. Sci. Eng.*, **5**(4), 68–78.

A. Nakano, M. E. Bachlechner, R. K. Kalia, E. Lidorikis, P. Vashishta, G. Z. Voyiadjis, T. J. Campbell, S. Ogata and F. Shimojo, 2001, Multiscale simulation of nanosystems. *Comp. Sci. Eng.*, **3**, 56–66.

A. Nakano, L. S. Bi, R. K. Kalia and P. Vashishta, 1994a, Molecular-dynamics study of the structural correlation of porous silica with use of a parallel computer. *Phys. Rev. B*, **49**, 9441–9452.

A. Nakano, R. K. Kalia and P. Vashishta, 1994b, Multiresolution molecular-dynamics algorithm for realistic materials modeling on parallel computers. *Comp. Phys. Commun.*, **83**, 197–214.

A. Nakano, R. K. Kalia and P. Vashishta, 1998b, Multilevel algorithms for large-scope molecular dynamics simulations of nanostructures on parallel computers. *VLSI Des.*, **8**, 123–128.

A. Nakano, P. Vashishta and R. K. Kalia, 1993, Parallel multiple-time-step molecular dynamics with three-body interaction. *Comp. Phys. Commun.*, **77**, 303–312.

A. Needleman, 2000, Computational mechanics at the mesoscale. *Acta Mater.*, **48**, 105–124.

T. G. Nieh, P. Luo, W. Nellis, D. Lesuer and D. Benson, 1996, Dynamic compaction of aluminum nanocrystals. *Acta Mater.*, **44**, 3781–3788.

H. Noguchi and Y. Furuya, 1997, A method of seamlessly combining a crack tip molecular dynamics enclave with a linear elastic outer domain in simulating elastic-plastic crack advance. *Int. J. Fract.*, **87**, 309–329.

C. D. Norton, J. Z. Lou and T. Cwik, 2001, Status and directions for the PYRAMID parallel unstructured AMR library. In: "8th Intl. Workshop on Solving

Irregularly Structured Problems in Parallel, San Francisco."

S. T. O'Connell and P. A. Thompson, 1995, Molecular dynamics–continuum hybrid computations: a tool for studying complex fluid flows. *Phys. Rev. E*, **52**, R5792–R5795.

M. Ortiz, A. M. Cuitino, J. Knap and M. Koslowski, 2001, Mixed atomistic-continuum models of material behavior: The art of transcending atomistics and informing continua. *MRS Bull.*, **26**, 216–221.

M. Ortiz and R. Phillips, 1999, Nanomechanics of defects in solids. *Adv. Appl. Mech.*, **35**, 1–79.

B. N. J. Persson, 1998, On the role of inertia and temperature in continuum and atomistic models of brittle fracture. *J. Phys.: Condens. Matter*, **10**, 10529–10538.

R. Phillips, 2001, Crystals, Defects, and Microstructures: Modeling Across Scales. Cambridge University Press, Cambridge, UK.

W. J. Phythian, R. E. Stoller, A. J. E. Foreman, A. F. Calder and D. J. Bacon, 1995, A comparison of displacement cascades in copper and iron by molecular dynamics and its application to microstructural evolution. *J. Nucl. Mater.*, **223**, 245–261.

J. H. Prevost, T. J. Baker, J. Liang and Z. Suo, 2001, A finite element method for stress-assisted surface reaction and delayed fracture. *Int. J. Solids Struct.*, **38**, 5185–5203.

D. Qian, G. J. Wagner, W. K. Liu, M.-F. Yu and R. S. Ruoff, 2002, Mechanics of carbon nanotubes. *Appl. Mech. Rev.*, Submitted.

H. Rafii-Tabar, L. Hua and M. Cross, 1998, A multi-scale atomistic-continuum modelling of crack propagation in a two-dimensional macroscopic plate. *J. Phys. Cond. Matter*, **10**, 2375–2387.

S. Rao, T. A. Parthasarathy and C. Woodward, 1999, Atomistic simulation of cross-slip processes in model FCC structures. *Philos. Mag. A*, **79**, 1167–1192.

R. Reigada, F. Sagués and J. M. Costa, 1994, A Monte-Carlo simulation of localized corrosion. *J. Chem. Phys.*, **101**, 2329–2337.

R. E. Rudd and J. Q. Broughton, 1998, Coarse-grained molecular dynamics and the atomic limit of finite elements. *Phys. Rev. B*, **58**, R5893–R5896.

R. E. Rudd and J. Q. Broughton, 2000, Concurrent coupling of length scales in solid state systems. *Phys. Stat. Sol. B*, **217**, 251–291.

S. Sako, K. Ohshima and T. Fujita, 1990, Surface oxide film of metallic small particle. *J. Phys. Soc. Japan*, **59**, 662–666.

J. C. Sánchez-López, A. Fernandez, C. F. Conde, A. Conde, C. Morant and J. M. Sanz, 1996, The melting behavior of passivated nanocrystalline aluminum. *Nanostruct. Mater.*, **7**, 813–822.

J. C. Sánchez-López, A. R. Gonzalez-Elipe and A. Fernandez, 1998, Passivation of nanocrystalline Al prepared by the gas phase condensation method: an X-ray photoelectron spectroscopy study. *J. Mater. Res.*, **13**, 703–710.

J. Schiøtz and A. E. Carlsson, 1997, Calculation of elastic Green's functions for lattices with cavities. *Phys. Rev. B*, **56**, 2292–2294.

V. B. Shenoy, R. Miller, E. B. Tadmor, R. Phillips and M. Ortiz, 1998, Quasicontinuum models of interfacial structure and deformation. *Phys. Rev. Lett.*, **80**, 742–745.

V. B. Shenoy, R. Miller, E. B. Tadmor, D. Rodney, R. Phillips and M. Ortiz, 1999, An adaptive finite element approach to atomic-scale mechanics: the quasicontinuum method. *J. Mech. Phys. Solids*, **47**, 611–642.

V. B. Shenoy, R. Phillips and E. B. Tadmor, 2000, Nucleation of dislocations beneath a plane strain indenter. *J. Mech. Phys. Solids*, **48**, 649–673.

R. W. Siegel, 1994, What do we really know about the atomic-scale structures of nanophase materials? *J. Phys. Chem. Solids*, **55**, 1097–1106.

G. B. Sinclair and G. Meda, 2001, On some anomalies in Lame's solutions for elastic solids with holes. *J. Appl. Mech.*, **68**, 132–134.

G. S. Smith, E. B. Tadmor, N. Bernstein and E. Kaxirast, 2001, Multiscale simulations of silicon nanoindentation. *Acta Mater.*, **49**, 4089–4101.

P. Sofronis, 1995, The influence of mobility of dissolved hydrogen on the elastic response of a metal. *J. Mech. Phys. Solids*, **43**, 1385–1407.

N. Soneda and T. D. de la Rubia, 1998, Defect Production, annealing kinetics and damage evolution in alpha-Fe: an atomic-scale computer simulation. *Phil. Mag. A*, **78**, 995–1019.

E. A. Stern, R. W. Siegel, M. Newville, P. G. Sanders and D. Haskel, 1995, Are nanophase grain boundaries anomalous? *Phys. Rev. Lett.*, **75**, 3874–3877.

F. H. Stillinger and T. A. Weber, 1985, Computer simulation of local order in condensed phases of silicon. *Phys. Rev. B*, **31**, 5262–5271.

F. H. Streitz and J. W. Mintmire, 1994, Electrostatic potentials for metal-oxide surfaces and interfaces. *Phys. Rev. B*, **50**, 11996–12003.

M. Strobel, K.-H. Heinig and T. Michely, 2001, Mechanisms of pit coarsening in ion erosion of FCC (1 1 1) surfaces: a kinetic 3-D lattice monte carlo study. *Surf. Sci.*, **486**, 136–156.

B. H. Suits, P. Apte, D. E. Wilken and R. W. Siegel, 1995, NMR study of nanophase Al/Al-oxide powder and consolidated composites. *Nanostruct. Mater.*, **6**, 609–612.

D. Sulsky, Z. Chen and H. L. Schreyer, 1994, A particle method for history-dependent materials. *Comp. Methods Appl. Mech. Eng.*, **118**, 179–196.

D. Sulsky and H. L. Schreyer, 1996, Axisymmetric form of the material point method with applications to upsetting and Taylor impact problems. *Comp. Meths. Appl. Mech. Eng.*, **139**, 409–429.

D. Sulsky, S-J. Zhou and H. L. Schreyer, 1995, Application of a particle-in-cell method to solid mechanics. *Comp. Phys. Commun.*, **87**, 236–252.

B. von Sydow and G. Wahnström, 1996, Lattice distortions around frozen and mobile hydrogen in niobium: a molecular-dynamics study. *Phys. Rev. B*, **53**, 3171–3176.

E. B. Tadmor, M. Ortiz and R. Phillips, 1996a, Quasi-continuum analysis of defects in solids. *Phil. Mag. A*, **73**, 1529–1563.

E. B. Tadmor, R. Phillips and M. Ortiz, 1996b, Mixed atomistic and continuum models of deformation in solids. *Langmuir*, **12**, 4529–4534.

H. Tan, 2001, A lattice material point method that can adaptively link continuum and atomistic simulations of fracture in nanocomposite ceramic. In: "6th US National Congress on Computational Mechanics, Dearborn, Michigan, Aug. 1–4."

H. Tan, 2002, Fracture simulations using material point method with broken cell shape functions. Submitted.

H. Tan and J. A. Nairn, 2002, Hierarchical, adaptive, material point method for dynamic energy release rate calculations. *Comp. Methods Appl. Mech. Eng.*, **191**, 2095–2109.

H. Tan and W. Yang, 1994a, Atomistic/continuum simulation of interfacial fracture: I. Atomistic simulation. *Acta Mech. Sinica*, **10**, 150–161.

H. Tan and W. Yang, 1994b, Atomistic/continuum simulation of interfacial fracture: II. Atomistic/dislocation/ continuum simulation. *Acta Mech. Sinica*, **10**, 237–249.

H. Tan and W. Yang, 1995, Nonlinear motion of crack tip atoms during dislocation emission processes. *J. Appl. Phys.*, **78**, 7026–7034.

H. Tan and W. Yang, 1996a, Nonlinear motion of crack tip atoms during cleavage processes. *Int. J. Fract.*, **77**, 199–212.

H. Tan and W. Yang, 1996b, Catastrophic fracture induced fracto-emission. *J. Mater. Sci.*, **31**, 2653–2660.

H. Tan and W. Yang, 1998, Toughening mechanisms of nano-composite ceramics. *Mech. Mater.*, **30**, 111–123.

Q. Tang and T. Wang, 1999, Dislocations emission and crack extension at the atomistic crack tip in body-centered-cubic metal Mo. *J. Mater. Res.*, **14**, 4035–4043.

R. Thomson, S. J. Zhou, A. E. Carlsson and V. K. Tewary, 1992, Lattice imperfections studied by use of lattice Green's functions. *Phys. Rev. B*, **46**, 10613–10622.

M. E. Tuckerman, G. J. Martyna and B. J. Berne, 1990, Molecular dynamics algorithm for condensed systems with multiple time scales. *J. Chem. Phys.*, **93**, 1287–1291.

P. Vashishta, M. Bachlechner, A. Nakano, T. J. Campbell, R. K. Kalia, S. Kodiyalam, S. Ogata, F. Shimojo and P. Walsh, 2001, Multimillion atom simulation of materials on parallel computers-nanopixel, interfacial fracture, nanoindentation and oxidation. *Appl. Surf. Sci.*, **182**, 258–264.

S. Veprek, 1999, The search for novel, superhard materials. *J. Vac. Sci. Technol. A*, **17**, 2401–2420.

S. Veprek and A. S. Argon, 2002, Towards the understanding of mechanical properties of super- and ultra-hard nanocomposites, *J. Vac. Sci. Technol. B*, **20**, 650–654.

W. Yang and H. Tan, 1996, Chaotic atom motion excited by fracture. *Mater. Sci. Res. Int.*, **2**, 1–12.

W. Yang, H. Tan and T. Guo, 1994, Evolution of crack tip process zones. *Modelling Simul. Mater. Sci. Eng.*, **2**, 767–782.

W. Yang, J.-C. Tang, Y.-S. Ing and C.-C. Ma, 2001, Transient dislocation emission from a crack tip. *J. Mech. Phys. Solids*, **49**, 2431–2453.

H. H. Yu and Z. Suo, 2000, Stress-dependent surface reactions and implications for a stress measurement technique. *J. Appl. Phys.*, **87**, 1211–1218.

H. Zhang and W. Yang, 1994, Three dimensional dislocation loops generated from a weak inclusion in a strained material heterostructure. *J. Mech. Phys. Solids*, **42**, 913–930.

Y. W. Zhang and A. F. Bower, 1999, Numerical simulations of island formation in a coherent strained epitaxial thin film system. *J. Mech. Phys. Solids*, **47**, 2273–2297.

Y. W. Zhang and T. C. Wang, 1995, Simulation of nucleation and emission of dislocations by molecular-dynamics method. *J. Appl. Phys.*, **77**, 2393–2399.

G. H. Zhou, F. X. Zhou, F. R. Wan and W. Y. Chu, 1998, Molecular dynamics simulation of hydrogen enhancing dislocation emission. *Key Eng. Mater.*, **145–149**, 123–128.

S. J. Zhou, D. M. Beazley, P. S. Lomdahl and B. L. Holian, 1997, Large-scale molecular dynamics simulations of three-dimensional ductile failure. *Phys. Rev. Lett.*, **78**, 479–482.

S. J. Zhou, A. E. Carlsson and R. Thomson, 1993, Dislocation nucleation and crack stability: lattice Green's-function treatment of cracks in a model hexagonal lattice. *Phys. Rev. B*, **47**, 7710–7719.

S. J. Zhou, P. S. Lomdahl, R. Thomson and B. L. Holian, 1996, Dynamic crack processes via molecular dynamics. *Phys. Rev. Lett.*, **76**, 2318–2321.